

# Turbulent secondary flows in wall turbulence: vortex forcing, scaling arguments, and similarity solution

William Anderson<sup>1</sup>  · Jianzhi Yang<sup>1,2</sup> · Kalyan Shrestha<sup>1</sup> · Ankit Awasthi<sup>1</sup>

Received: 28 August 2017 / Accepted: 27 April 2018 / Published online: 16 May 2018  
© Springer Science+Business Media B.V., part of Springer Nature 2018

**Abstract** Spanwise surface heterogeneity beneath high-Reynolds number, fully-rough wall turbulence is known to induce a mean secondary flow in the form of counter-rotating streamwise vortices—this arrangement is prevalent, for example, in open-channel flows relevant to hydraulic engineering. These counter-rotating vortices flank regions of predominant excess(deficit) in mean streamwise velocity and downwelling(upwelling) in mean vertical velocity. The secondary flows have been definitively attributed to the lower surface conditions, and are now known to be a manifestation of Prandtl’s secondary flow of the second kind—driven and sustained by spatial heterogeneity of components of the turbulent (Reynolds averaged) stress tensor (Anderson et al. J Fluid Mech 768:316–347, 2015). The spacing between adjacent surface heterogeneities serves as a control on the spatial extent of the counter-rotating cells, while their intensity is controlled by the spanwise gradient in imposed drag (where larger gradients associated with more dramatic transitions in roughness induce stronger cells). In this work, we have performed an order of magnitude analysis of the mean (Reynolds averaged) transport equation for streamwise vorticity, which has revealed the scaling dependence of streamwise circulation intensity upon characteristics of the problem. The scaling arguments are supported by a recent numerical parametric study on the effect of spacing. Then, we demonstrate that mean streamwise velocity can be predicted a priori via a similarity solution to the mean streamwise vorticity transport equation. A vortex forcing term has been used to represent the effects of spanwise topographic heterogeneity within the flow. Efficacy of the vortex forcing term was established with a series of large-eddy simulation cases wherein vortex forcing model parameters were altered to capture different values of spanwise spacing, all of which demonstrate that the model can impose the effects of spanwise topographic heterogeneity (absent the need to actually model roughness elements); these results also justify use of the vortex forcing model in the similarity solution.

---

✉ William Anderson  
wca140030@utdallas.edu

<sup>1</sup> Mechanical Engineering Department, The University of Texas at Dallas, Richardson, TX, USA

<sup>2</sup> Mechanical Engineering Department, Hefei University of Technology, Hefei, China

**Keywords** Turbulence · Vortex forcing model · Streamfunction

## 1 Introduction

Inertia-dominated, rough-wall turbulence is the norm in many engineering and geophysical flows of practical importance [1–3]. Under such conditions, the spatial distribution of momentum-absorbing elements results in elevated turbulence production, which enhances the cumulative aero-/hydro-dynamic signature of the surface (i.e., the shear velocity,  $u_\tau$ ). This process is mechanistically driven by flow separation from individual elements, and is thus confined to the layer of fluid immediately above the surface—the roughness sublayer [4]. The roughness sublayer thickness scales linearly with aggregate element height. Turbulence within the roughness sublayer is structurally autonomous to the above inertial layer, with the flow exhibiting scaling that indicates greater resemblance to a mixing layer [5–7] (dynamic autonomy is another matter, with recent findings suggesting that the roughness sublayer is subjected to an amplitude modulation via dynamics of the inertial layer [8–10]).

When the aggregate element height is sufficiently “small”, and the spatial distribution of elements is relatively homogeneous, outer-layer similarity is valid [11] and the structural nature of the turbulence is equivalent to a smooth wall [12–15]. However, we stress recent results from Hong et al. [16], who showed that outer-layer perturbations can be detected in the power spectral density of streamwise velocity fluctuations, with a series of clear spectral peaks evident at wavelengths corresponding precisely with characteristic scales of the underlying topography; their data was attained via experimental measurement of turbulent flow over a topography that thoroughly conforms to all antecedent requirements for presumption of outer-layer similarity. The specific definition of “small” is itself the topic of ongoing research, although  $H/h > 30$  is a widely-cited condition for outer-layer similarity [2, 14], where  $H$  and  $h$  represent the flow depth and aggregate element height, respectively. For  $H/h < 30$ , the outer layer is perturbed by shear layers and wakes originating within the roughness sublayer. Similarly, the specific conditions for surface spatial homogeneity is itself an open problem [17, 18], with the planform area index,  $\lambda_p$ , commonly used to define “sparseness” [19].

Streamwise and spanwise surface heterogeneities are relevant to the present discussion (herein, we adopt the nomenclature,  $\mathbf{x} = x_1\hat{i} + x_2\hat{j} + x_3\hat{k}$ , where the first, second, and third component of any vector represents its streamwise, spanwise, and wall-normal value, respectively). Turbulent wall flows respond to the former with elevated turbulence production in the fluid proximal to the heterogeneity and the formation of an internal layer—the internal boundary layer (IBL)—which grows in thickness in the downflow direction [20–23]. The IBL has received substantial attention from the community, where some have developed prognostic schemes for thickness of the internal layer based on the magnitude of surface change [17]. The latter—spanwise surface heterogeneity—has received far less attention. Recently, however, there has been growing interest in this problem and its affect on dynamics of the above turbulent flow [24–34].

The topic of surface heterogeneities is relevant to a variety of high Reynolds number environmental flows. For example, efforts to characterize atmospheric boundary layer flows over heterogeneous landscapes [35]. In addition, there remains substantial interest in open-channel hydraulic flows and the emergent secondary flow patterns when the lower surface exhibits spanwise heterogeneities [24, 26, 36]. It is now well understood that spanwise surface heterogeneity alters the structure of the above flow due to a spanwise variation in imposed surface stress. This variation in imposed surface stress is responsible for altering

the spatial distribution of turbulent stresses in the spanwise–wall-normal plane. These flows exhibit a prominent downwelling and upwelling above the high and low roughness, respectively, and these locations have been named high- and low-momentum pathways (HMP, LMP), respectively [25, 29]. Anderson et al. [31] demonstrated that the flows were a manifestation of Prandtl’s secondary flow of the second kind [37], in accordance with aforementioned contributions from the river hydraulics community. This was accomplished by leveraging techniques commonly used by those studying secondary flows in turbulent duct flows [37–43]. And while preceding studies have confirmed that mean secondary flows in channels and boundary layers are a manifestation of Prandtl’s secondary flow of the second kind [37, 42], open questions on the intensity of secondary flows with spacing remain [32], and development of prognostic tools for such flows is of interest.

Vanderwel and Ganapathisubramani [30] have recently shown that spacing between adjacent heterogeneities serves as a control on the depth of the resulting mean circulations. Yang and Anderson [32] performed a comprehensive parametric study on the influence of spacing,  $s_2/H$ , and element height,  $h/H$ . They argued that when  $H/h \gtrsim 20$ , spacing is itself a flow parameter. When  $s_2/H \gtrsim 2$ , two circular counter-rotating cells can freely occupy the domain, and the surface has the aero-/hydro-dynamic signature of a topography. For  $s_2/H \lesssim 2$ , secondary cells can not occupy the domain since they are attenuated by adjacent rolls [30], and the surface has the aero-/hydro-dynamic signature of a roughness.

## 1.1 Present study

The authors have studied the Reynolds-averaged momentum and streamwise vorticity transport equation to explain some of the phenomena observed in these flows when perturbed by spanwise surface heterogeneity. In Sect. 2, the transport equations and a scaling analysis of the Reynolds-averaged streamwise vorticity transport equation has been used to explain the trends observed in the intensity of counter-rotating secondary flows with varying spanwise spacing (this component of the research leverages results presented in the recent article, Yang and Anderson [32]). With this, in Sect. 3 we recast the Reynolds-averaged streamwise vorticity transport equation as an ordinary differential equation (ODE) via introduction of a similarity variable; this similarity solution allows a priori computation of the mean streamwise velocity distribution due to a pre-defined model for the counter-rotating cells. The similarity solution is tested with a series of test cases (Sect. 4), with results shown in Sect. 5. Section 6 shows results from complementary large-eddy simulation (LES) of flow over a homogeneous roughness, but with an additional body force that parametrizes spanwise topographic heterogeneity effects (this section is largely intended to demonstrate efficacy of key aspects of the developments in Sects. 2 and 3). The results are consistent with all preceding observations on the spatial nature and intensity of these flows, and thus justify the vortex forcing approach and the theoretical deductions. We expect that prognostic description of Reynolds-averaged flows perturbed by such spanwise heterogeneous conditions will have implications for hydraulic design applications, for example. The results could also prove useful for initializing high-resolution numerical simulations as a means to define the Reynolds-averaged flow a priori. Concluding remarks are provided in Sect. 7. The developments in Sects. 2 and 3 are predicated upon three enabling conditions:

1. The secondary flow is sustained via a vortex body force,  $\mathbf{f}^\omega$ . The vortex forcing model is inspired by efforts to model Langmuir turbulence in the ocean mixed layer with the Craik-Leibovich transport equations [44–50] and introduction of the Stokes drift

profile [51]. As comprehensively outlined below, we adopt a spanwise-variable version of this model, where the model is tuned to align with the presence of downwelling and upwelling and, thus, impart the same affects as a spanwise variation in surface stress.

2. The similarity solution makes use of a streamfunction,  $\psi(x_2, x_3)$ , to represent the counter-rotating streamwise cells flanking regions of streamwise momentum excess/deficit. We make use of a candidate streamfunction in order to demonstrate efficacy of the formalism, although other models could certainly be used without loss of generality.
3. As will be shown, a turbulent viscosity is required to capture the influence of turbulent stress heterogeneity upon evolution of vorticity (referred to hereafter as turbulent torque, and studied in Mansfield et al. [52, 53]). For the present purposes, we will assume that the turbulent viscosity can be set equivalent to the product of flow depth and shear velocity, although one could further generalize the procedure for alternative, more sophisticated models. Such generalizations would not result in changes to the similarity solution.

We varied parameters of the model to replicate different forcing conditions, which demonstrated how the intensity of the counter-rotating cells and the prominence of the HMPs and LMPs varies. We note some conceptual similarities between the present work and the contributions from McKeon et al., who presented models for the elongated structures in turbulent Couette flow (see, for example, Gayme et al. [54]). However, the present work is distinctly different as the results are derived from consideration of the Reynolds-averaged streamwise vorticity transport equation, and because here we have used a similarity solution as a prognostic tool to quantify the resultant mean flow in response to spanwise topographic heterogeneity. For completeness, we also point out that for transitional boundary layers, Townsend [11] developed a prognostic tool for the onset of persistent rolls originating from lateral stress variations. This prognostic tool was derived from the Reynolds-averaged vorticity transport equation—the equation underpinning this work—but was used for an entirely different purpose (here, spanwise surface-stress variation is imposed via a proxy model for topographic heterogeneity, and we are concerned with inertial-dominated flows).

## 2 Vorticity dynamics

We will consider the Reynolds-averaged transport equations for momentum,  $\rho\langle\mathbf{u}\rangle_t$ , and vorticity,  $\langle\boldsymbol{\omega}\rangle_t$ , where both vectors are presumed solenoidal in the present development, i.e.  $\nabla \cdot \langle\mathbf{u}\rangle_t = \nabla \cdot \langle\boldsymbol{\omega}\rangle_t = 0$ , and where a Reynolds-averaged quantity is denoted by  $\langle\ldots\rangle_t$ . We introduce a model to parametrize the role of spanwise topographic heterogeneity (model efficacy is demonstrated in Sect. 6). We go on to perform an order of magnitude analysis of the Reynolds-averaged vorticity transport equation with characteristic scales relevant to the “roughness” or “topography” regime, as highlighted in Yang and Anderson [32]. The majority of this development is devoted to a channel (internal) flow, although there is no evidence to suggest that the approach would not be valid for a boundary layer if the streamwise heterogeneity can be compensated for (or simply neglected, as has been done with success in preceding studies such as Willingham et al. [27] and Anderson et al. [31], who have argued that the effect of streamwise heterogeneity is small compared with other influences). The approach is applied for  $\mathbf{x} \in \Omega$ , with boundary conditions outlined below.

## 2.1 Transport equations with vortex forcing

Consider the forced Reynolds-averaged momentum transport equation:

$$\frac{D\langle \mathbf{u} \rangle_t}{Dt} = -\frac{1}{\rho} \nabla p - \nabla \cdot \langle \mathbf{T} \rangle_t - \mathbf{e}_1 \Pi + \langle \mathbf{f}^\omega \rangle_t, \quad (1)$$

where  $\langle \mathbf{T} \rangle_t = \langle \mathbf{u}' \otimes \mathbf{u}' \rangle_t$  is the Reynolds (total) turbulent stress tensor,  $\mathbf{u}' = \mathbf{u} - \langle \mathbf{u} \rangle_t$ , and  $\Pi = -\rho u_\tau^2 H^{-1}$  is an imposed pressure gradient, where  $u_\tau$  is imposed shear velocity,  $\rho$  is fluid density, and  $H$  is flow depth. The final term on the right-hand side of Eq 1 is a body force, computed here via introduction of an  $x_2$ - $x_3$  dependent forcing velocity, *vis*:

$$\langle \mathbf{f}^\omega \rangle_t = \langle \boldsymbol{\omega} \rangle_t \times \mathbf{u}^s, \quad (2)$$

where  $\langle \boldsymbol{\omega} \rangle_t = \nabla \times \langle \mathbf{u} \rangle_t$  is Reynolds-averaged vorticity and  $\mathbf{u}^s$  is a forcing velocity used to impose the effects of spanwise variable surface stress,

$$\mathbf{u}^s = \left\{ U^s \left( \exp \left[ -\frac{x_2^2}{\alpha_1 H^2} \right] - \exp \left[ -\frac{\{x_2 - \lambda\}^2}{\alpha_1 H^2} \right] \right) \exp \left( -\frac{x_3^2}{\alpha_2 H^2} \right), 0, 0 \right\}, \quad (3)$$

where  $U^s$  is a magnitude. This vortex forcing model is inspired by efforts to model Langmuir turbulence in the ocean upper-mixed layer via the Craik-Leibovich equations [46–48]. Unlike the traditional applications to modeling Langmuir turbulence, however, the transport equations are not subjected to wave averaging in order to capture the aggregate effects associated with wave orbital dynamics. The  $\mathbf{u}^s$  exhibits an exponential decline in the wall-normal ( $x_3$ ) direction, which ensures that the input vortex forcing effects are more pronounced near the wall and gradually approach channel-like conditions in the outer (consistent with preexisting knowledge on low- and high-momentum pathways). The more radical condition is introduction of the spanwise ( $x_2$ ) dependence, which is altered via a tuning parameter,  $\alpha_1$ . The spanwise dependence is necessary to capture spanwise variability in drag and momentum that is the signature of low- and high-momentum pathways [31]. The model used here was designed in coordination with the vortex forcing model, where expansion of Eq. 2 provides guidance on the model configuration (as will be shown later, this forcing arrangement yields qualitatively-similar results when implemented during complementary large-eddy simulation. Equation 3 provides a means to spatially fix the position of rotating cells. Note that the spanwise surface heterogeneity due to rows of obstacles could also be represented via, for example, an immersed-boundary method wherein the Eq. 1 body force is,  $f \sim (\mathbf{u} \cdot \mathbf{u}) h^{-1}$ , and where  $h$  is the element height. But, this approach requires an immersed-boundary method, as opposed to the relative simplicity offered by Eq. 2.

The Reynolds-averaged vorticity transport equation is attained by evaluating the curl of Eq. 1, yielding:

$$\frac{D\langle \boldsymbol{\omega} \rangle_t}{Dt} = \langle \boldsymbol{\omega} \rangle_t \cdot \nabla \langle \mathbf{u} \rangle_t - \nabla \times (\nabla \cdot \langle \mathbf{T} \rangle_t) + \nabla \times \langle \mathbf{f}^\omega \rangle_t, \quad (4)$$

where the pressure gradient,  $\nabla p$ , and pressure gradient forcing,  $\mathbf{e}_1 \Pi$ , vanish through the curl operation since they are both spatially uniform. The first, second, and third right-hand side terms are vortex stretching and tilting, turbulent torque, and vortex forcing, respectively. Note that Prandtl's secondary flows of the first and second kind are driven by the first and second right-hand side terms, respectively [42].

Here, we are interested only in the streamwise ( $x_1$ ) component of Eq. 4:

$$\frac{D\langle\omega_1\rangle_t}{Dt} = \langle\omega_i\rangle_t \partial_i \langle u_1 \rangle_t - \epsilon_{1qi} \partial_q \partial_j \langle T_{ji} \rangle_t + \epsilon_{1jk} \partial_j \langle f_k^\omega \rangle_t. \quad (5)$$

For applications to turbulent channel and pipe flows with spanwise surface heterogeneity (owing to topographic forcing) but streamwise homogeneity, all streamwise derivatives vanish [27, 31]. With this condition, we immediately deduce that the stretching and tilting term,  $\langle\omega_i\rangle_t \partial_i \langle u_1 \rangle_t = \langle\omega_1\rangle_t \partial_1 \langle u_1 \rangle_t + \langle\omega_2\rangle_t \partial_2 \langle u_1 \rangle_t + \langle\omega_3\rangle_t \partial_3 \langle u_1 \rangle_t$ , vanishes upon substitution of the vorticity components,  $\langle\omega\rangle_t = \{\partial_2 \langle u_3 \rangle_t - \partial_3 \langle u_2 \rangle_t, \partial_3 \langle u_1 \rangle_t - \partial_1 \langle u_3 \rangle_t, \partial_1 \langle u_2 \rangle_t - \partial_2 \langle u_1 \rangle_t\}$ . The final right-hand side term,

$$\begin{aligned} \epsilon_{1jk} \partial_j \langle f_k^\omega \rangle_t &= \epsilon_{1jk} \partial_j \epsilon_{kpq} \langle \omega_p \rangle_t u_q^s = \delta_{1p} \delta_{jq} \partial_j \langle \omega_p \rangle_t u_q^s - \delta_{1q} \delta_{jp} \partial_j \langle \omega_p \rangle_t u_q^s \\ &= \partial_j \langle \omega_1 \rangle_t u_j^s - \partial_j \langle \omega_j \rangle_t u_1^s, \end{aligned} \quad (6)$$

simplifies greatly upon application of  $\partial_1() = 0$ , resulting finally in:

$$\epsilon_{1jk} \partial_j \langle f_k^\omega \rangle_t = (\partial_2 \langle u_1 \rangle_t) (\partial_3 u_1^s) - (\partial_3 \langle u_1 \rangle_t) (\partial_2 u_1^s), \quad (7)$$

where  $u^s$  is a pre-defined vortex forcing model input argument, defined here with the Eq. 3 model. The second right-hand side term, herein called turbulent torque, can be expressed in two ways [52, 53]. Firstly, after substitution of the components of  $\langle T \rangle_t$ :

$$\epsilon_{1qi} \partial_q \partial_j \langle T_{ji} \rangle_t = (\partial_2^2 - \partial_3^2) \langle T_{23} \rangle_t + \partial_{23} (\langle T_{33} \rangle_t - \langle T_{22} \rangle_t). \quad (8)$$

However, for the present purposes wherein we are concerned with the scale of right-hand side terms appearing in Eq. 5, it is more convenient to introduce the Boussinesq model [55]:

$$\mathbf{T} = -2\nu_t \left( \mathbf{S} - \frac{2}{3} \nabla \cdot \langle \mathbf{u} \rangle_t \boldsymbol{\delta} \right) + \frac{2}{3} \boldsymbol{\delta} k, \quad (9)$$

where  $\nu_t$  is a turbulent (eddy) viscosity,  $\mathbf{S} = \frac{1}{2} (\nabla \langle \mathbf{u} \rangle_t + \nabla \langle \mathbf{u} \rangle_t^T)$  is the strain-rate tensor and  $k = \frac{1}{2} \langle \mathbf{u}' \rangle_t : \langle \mathbf{u}' \rangle_t$  is turbulent kinetic energy. For the present solenoidal flow,  $\nabla \cdot \langle \mathbf{u} \rangle_t = 0$ , and Eq. 9 reduces to  $\mathbf{T} = -2\nu_t \mathbf{S} + \frac{2}{3} \boldsymbol{\delta} k$ , and substitution into Eq. 8 yields the somewhat simplified expression for turbulent torque (with the caveat that  $\nu_t$  must be defined a priori):

$$\epsilon_{1qi} \partial_q \partial_j \langle T_{ji} \rangle_t = -\frac{1}{2} \nu_t (\partial_3^2 \langle \omega_1 \rangle_t + \partial_2^2 \langle \omega_1 \rangle_t). \quad (10)$$

Substitution of the Eqs. 7 and 10 relations into Eq. 5 yields:

$$\begin{aligned} &\langle u_2 \rangle_t \partial_2 \langle \omega_1 \rangle_t + \langle u_3 \rangle_t \partial_3 \langle \omega_1 \rangle_t \\ &= \frac{1}{2} \nu_t (\partial_3^2 \langle \omega_1 \rangle_t + \partial_2^2 \langle \omega_1 \rangle_t) + (\partial_2 \langle u_1 \rangle_t) (\partial_3 u_1^s) \\ &\quad - (\partial_3 \langle u_1 \rangle_t) (\partial_2 u_1^s). \end{aligned} \quad (11)$$

Note that, as one would anticipate, the curl of the vortex forcing term (Eq. 2) enters only on the right-hand side of the equation governing transport of  $\langle \omega_1 \rangle_t$ , i.e.,

$$\langle \mathbf{u} \rangle_t \cdot \nabla \langle \omega_2 \rangle_t = \langle \omega \rangle_t \cdot \nabla \langle u_2 \rangle_t + v_t \nabla^2 \langle \omega_2 \rangle_t, \quad (12)$$

and,

$$\langle \mathbf{u} \rangle_t \cdot \nabla \langle \omega_3 \rangle_t = \langle \omega \rangle_t \cdot \nabla \langle u_3 \rangle_t + v_t \nabla^2 \langle \omega_3 \rangle_t. \quad (13)$$

## 2.2 Scaling arguments

A preceding study [32] has shown how the intensity of spanwise heterogeneous topographically-forced circulations changes as the spacing between elements varies. The authors used circulation, compensated for the presence of counter-rotating cells:

$$\Gamma^* = (u_t H)^{-1} \int_{\mathcal{A}} |\langle \omega_1 \rangle_t(x_2, x_3)| d^2 \mathbf{x}, \quad (14)$$

where  $d^2 \mathbf{x}$  represents the spanwise–wall-normal plane. The profile of  $\Gamma^*$  versus spanwise spacing,  $s_2/H$ , exhibits two distinct regions. For  $0 \leq s_2/H \lesssim 1$ ,  $\Gamma^*$  rises abruptly due to the growing spatial extent of counter-rotating cells (consistent with findings from Vanderwel and Ganapathisubramani [30]). For  $s_2/H \gtrsim 1$ ,  $\Gamma^*$  declines, although with a weaker dependence on  $s_2/H$ . We [32] have labeled these regions as “roughness” and “topography”, respectively, and demonstrated that the former does not inhibit outer-layer similarity, while the larger roll cells globally disrupt the flow such that outer-layer similarity is not possible. It would be of interest, then, to consider how the magnitude of constituent terms within Eq. 11 vary, and if this variation can be used to explain the observations of turbulent secondary flow intensity. Here, owing to the vortex forcing scheme, we use the symbol,  $\lambda$ , as an analog for  $s_2/H$ , while other characteristics of the problem are used to explain the observed  $\Gamma^* \sim \lambda^n$  scaling arguments. Since the flow regime is undeniably predicated upon spacing, we have decomposed the scaling exercises based on the aforementioned roughness and topography regimes.

### 2.2.1 Roughness

Under the roughness regime, we envision the following scales for terms in Eq. 11:

$$\langle u_1 \rangle_t \sim U, \langle u_2 \rangle_t \sim V, \langle u_3 \rangle_t \sim W, x_2 \sim \lambda, x_3 \sim \lambda, \mathbf{u}^s \sim U^s, \quad (15)$$

where  $U$ ,  $V$ , and  $W$  are scales for the streamwise, spanwise, and vertical velocity, respectively; for simplicity, we will leverage the circular form of secondary rolls by stating that  $x_2 \sim x_3 \sim \lambda$ .  $U^s$  is the amplitude of the Stokes forcing velocity (Eq. 3), and thus sets the magnitude of the vortex forcing (Eq. 7). Upon substitution into Eq. 11, we attain:

$$V \frac{\langle \omega_1 \rangle_t}{\lambda}, W \frac{\langle \omega_1 \rangle_t}{\lambda}, v_t \frac{\langle \omega_1 \rangle_t}{\lambda^2}, v_t \frac{\langle \omega_1 \rangle_t}{\lambda^2}, \frac{UU^s}{\lambda^2}, \frac{UU^s}{\lambda^2}. \quad (16)$$

Dividing each term by  $U$  eliminates the advective terms since  $U/V \sim U/W > 1$  (this has been confirmed in turbulent ducts, boundary layers, and channels). Further algebra yields the relation:

$$\langle \omega_1 \rangle_t \sim \frac{U^s U}{v_t}, \quad (17)$$

which, upon substitution in Eq. 14 and presuming that  $d^2x \sim \lambda^2$ , yields:

$$\Gamma^* \sim \frac{U^s U}{u_\tau^2} S^2, \quad (18)$$

where  $S = \lambda/H$ . For simplicity and given its relatively immaterial importance to the present development, we have taken the liberty of setting  $v_t \sim u_\tau H$  in the transition from Eq. 16 to 17. This assumption is supported by recalling Eq. 9, the Boussinesq model upon which the Reynolds stresses can be related to the strain-rate tensor. Since the left- and right-hand side of Eq. 9 go like  $u_\tau^2$  and  $v_t H^{-1} u_\tau$ , respectively, it follows that  $v_t \sim u_\tau H$ . The prefactor,  $U_s U / u_\tau^2$ , plays the important role of representing the relative influence of the imposed Stokes drag. This factor may be thought of as a proxy for the roughness height,  $h/H$ , although such a connection can not strictly be made since the presence of momentum-absorbing elements has been parametrized via the vortex forcing,  $f^\omega$ , in Eqs. 1 and 4.

### 2.2.2 Topography

Under the topography regime, we envision the following scales for terms in Eq. 11:

$$\langle u_1 \rangle_t \sim U, \langle u_2 \rangle_t \sim V, \langle u_3 \rangle_t \sim W, x_2 \sim HS^{-1}, x_3 \sim H, u^s \sim U^s, \quad (19)$$

where  $x_2 \sim HS^{-1}$  accounts for the fact that for very large  $S$ , adjacent counter-rotating secondary cells will be separated by a large region wherein the flow scales as a high Reynolds number channel flow. Upon substitution of the Eq. 19 scales, Eq. 11 reduces to:

$$V \frac{\langle \omega_1 \rangle_t}{HS^{-1}}, W \frac{\langle \omega_1 \rangle_t}{H}, v_t \frac{\langle \omega_1 \rangle_t}{H^2 S^{-2}}, v_t \frac{\langle \omega_1 \rangle_t}{H^2}, \frac{UU^s}{H^2 S^{-1}}, \frac{UU^s}{H^2 S^{-1}}. \quad (20)$$

As per the Sect. 2.2.1 development, division by  $U$  eliminates the advective terms since  $V/U \sim W/U \ll 1$ . Further algebra results in:

$$\langle \omega_1 \rangle_t \sim \frac{U^s U}{v_t}. \quad (21)$$

Substitution into Eq. 14 and using consistent scaling for the topography regime,  $d^2x \sim H^2 S^{-1}$ , where the  $S^{-1}$  factor accounts for the diminishing spatial extent occupied by cells as spacing increases, yields:

$$\Gamma^* \sim \frac{U^s U}{u_\tau^2} S^{-1}. \quad (22)$$

## 2.3 Summary

In summary, the analysis has indicated the following scaling for compensated circulation:

$$\Gamma^* \sim \begin{cases} \frac{U^s U}{u_\tau^2} S^2 & \text{if } S \lesssim 2, \text{ and} \\ \frac{U^s U}{u_\tau^2} S^{-1} & \text{if } S \gtrsim 2. \end{cases} \quad (23)$$

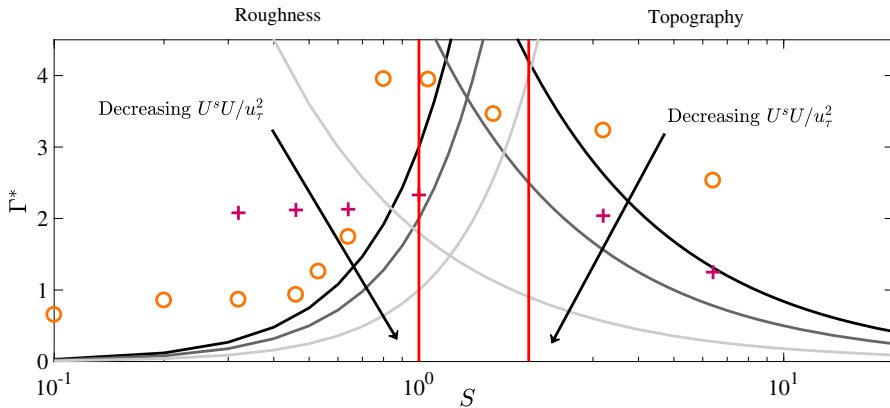


**Fig. 1** Equation 23 profiles for  $U^s U / u_\tau^2 = 3$  (black lines),  $U^s U / u_\tau^2 = 2$  (intermediate gray), and  $U^s U / u_\tau^2 = 1$  (light gray), for varying  $S = \lambda H^{-1}$ . Profiles increasing and decreasing with  $S$  are for the roughness regime (Eq. 18) and topography regime (Eq. 22), respectively. We have provided annotation of the ‘Roughness’ and ‘Topography’ regime  $S$  values, for discussion. Included also are discrete data points from [32], who performed an LES-based parametric study on the effects of element height and spanwise spacing,  $s_2/H$ . The orange circles and red ‘+’ signs correspond with elements with  $H/h = 15$  and  $H/h = 20$ , respectively (see “Appendix A” for additional discussion). Here, we have assumed  $S = s_2/H$ , while the red and orange symbols denote  $H/h = 20$  and  $15$ , respectively

It is interesting to note that  $\Gamma^* \sim U^s U / u_\tau^2$ , irrespective of the regime. Recall, however, that the Stokes drift magnitude is an indicator of the topography attributes—not the spanwise distance between adjacent rows of such elements—and there is thus no reason to expect the dependence of  $U^s$  to vary with  $S$ . Figure 1 shows the Eq. 23 scaling arguments for  $U^s U / u_\tau^2$  values summarized within the caption. We have plotted profiles for different values of  $U^s / U$ , which demonstrates the interplay between Stokes forcing and outer momentum. Moreover, the figure includes discrete datapoints for  $\Gamma^*$  against spanwise spacing,  $s_2/H$ , from the recent study by Yang and Anderson [32]. For that study, LES with an immersed-boundary method was used to model flow over rows of streamwise-aligned, vertically-truncated pyramid obstacles, where the rows were spaced at different  $s_2/H$  (see “Appendix A” for further discussion). Two sets of simulations were considered, where the element height was varied between the two sets ( $H/h = 15$  and  $H/h = 20$ ), while  $s_2/H$  was varied within each set. The datapoints do not exactly follow a single Eq. 23 profile, although there is no reason why they should owing to intrinsic differences between the simulations [32] and the present Stokes forcing approach. Moreover, the Yang and Anderson [32] study made use of a large number of simulations, and the results in some cases may be affected by mild non-stationarity in the simulations [56, 57]. Nonetheless, there is reasonable agreement in the trends between the scaling arguments and datapoints.

### 3 Similarity solution

Having used the preceding scaling arguments to demonstrate how the intensity of topographically-driven counter-rotating vortices varies with vortex forcing magnitude and spacing, we turn now to a prognostic solution for the corresponding streamwise velocity (i.e., the momentum excess or deficit within a HMP or LMP, respectively). This is derived

from the Reynolds-averaged streamwise vorticity transport equation (Eq. 11). Here, we present a similarity solution for  $\langle u_1 \rangle_t(x_2, x_3)$  based on introduction of a streamfunction for the counter-rotating circulations,  $\psi(x_2, x_3)$ . We introduce the similarity variable:

$$\eta = \eta(U^s, u_\tau, \lambda, x_2, x_3, H) = \frac{U^s}{u_\tau} G(x_2, x_3, \lambda, H), \quad (24)$$

where the function,  $G = G(x_2, x_3, \lambda, H)$ , exhibits an intrinsic dependence on the pre-defined streamfunction and, therefore, will be defined later in the development. Since  $\langle u_2 \rangle_t = \partial_3 \psi$ ,  $\langle u_3 \rangle_t = -\partial_2 \psi$ , and  $\langle \omega_1 \rangle_t = -\nabla^2 \psi = -\partial_2^2 \psi - \partial_3^2 \psi$ , Eq. 11 can be expressed as:

$$\begin{aligned} \partial_2 \psi (\partial_{223} \psi + \partial_{333} \psi) - \partial_3 \psi (\partial_{222} \psi + \partial_{233} \psi) = & -\frac{1}{2} v_t (\partial_{2222} \psi + 2\partial_{2233} \psi + \partial_{3333} \psi) \\ & + (\partial_2 \langle u_1 \rangle_t) (\partial_3 u_1^s) \\ & - (\partial_3 \langle u_1 \rangle_t) (\partial_2 u_1^s). \end{aligned} \quad (25)$$

In Eq. 25, the unknown quantities ( $\psi$  and  $\langle u_1 \rangle_t$ ) may be expressed with respect to the Eq. 24 similarity variable as:

$$\psi = u_\tau H \Psi(\eta), \quad (26)$$

and,

$$\langle u_1 \rangle_t = u_\tau U(\eta), \quad (27)$$

which yields, upon substitution in Eq. 25:

$$\begin{aligned} \partial_2 \Psi (\partial_{223} \Psi + \partial_{333} \Psi) - \partial_3 \Psi (\partial_{222} \Psi + \partial_{233} \Psi) + \frac{1}{2} (\partial_{2222} \Psi + 2\partial_{2233} \Psi + \partial_{3333} \Psi) \\ = u_\tau^{-1} H^{-2} [(\partial_2 U) (\partial_3 u_1^s) - (\partial_3 U) (\partial_2 u_1^s)]. \end{aligned} \quad (28)$$

In the transition from Eqs. 25 to 28, the model,  $v_t = u_\tau H$ , has been introduced in order to advance the development. This assumption, rudimentary though it is, exhibits consistency with the underlying Boussinesq model and enables the development to proceed; of course, more complex generalizations could be adopted, but such efforts are secondary to the focus of this work and not expected to materially alter trends derived from the similarity solution. “Appendix B” presents step-by-step evaluation of terms in Eq. 28, where use has been made of the univariate and multivariate Faà di Bruno formula [58, 59]. Evaluation of the partial derivatives in Eq. 28 yields:

$$\frac{dU}{d\eta} = A \frac{d^4 \Psi}{d\eta^4} + B \frac{d^3 \Psi}{d\eta^3} + C \frac{d^2 \Psi}{d\eta^2} + D \frac{d^2 \Psi}{d\eta^2} \frac{d\Psi}{d\eta} + E \frac{d\Psi}{d\eta} \frac{d\Psi}{d\eta} + F \frac{d\Psi}{d\eta}, \quad (29)$$

where the prefactors,  $A$ ,  $B$ ,  $C$ ,  $D$ ,  $E$ , and  $F$ , are:

$$A = \frac{1}{2} u_\tau H^2 \frac{([\partial_2 \eta]^2 + [\partial_3 \eta]^2)^2}{\partial_2 \eta \partial_3 u_1^s - \partial_3 \eta \partial_2 u_1^s}, \quad (30)$$

$$B = u_\tau H^2 \frac{\partial_{22}\eta [3\{\partial_2\eta\}^2 + \{\partial_3\eta\}^2] + \partial_{33}\eta [3\{\partial_3\eta\}^2 + \{\partial_2\eta\}^2] + 4\partial_2\eta\partial_3\eta\partial_{23}\eta}{\partial_2\eta\partial_3u_1^s - \partial_3\eta\partial_2u_1^s}, \quad (31)$$

$$C = u_\tau H^2 \frac{2\partial_2\eta[\partial_{222}\eta + \partial_{332}\eta] + 2\partial_3\eta[\partial_{333}\eta + \partial_{223}\eta] + 2[\partial_{23}\eta]^2 + \partial_{22}\eta\partial_{33}\eta}{\partial_2\eta\partial_3u_1^s - \partial_3\eta\partial_2u_1^s}, \quad (32)$$

$$D = u_\tau H^2 \frac{\partial_{23}\eta [\{\partial_2\eta\}^2 - \{\partial_3\eta\}^2] + \partial_2\eta\partial_3\eta[\partial_{33}\eta - \partial_{22}\eta]}{\partial_2\eta\partial_3u_1^s - \partial_3\eta\partial_2u_1^s}, \quad (33)$$

$$E = u_\tau H^2 \frac{\partial_2\eta[\partial_{223}\eta + \partial_{333}\eta] - \partial_3\eta[\partial_{222}\eta + \partial_{332}\eta]}{\partial_2\eta\partial_3u_1^s - \partial_3\eta\partial_2u_1^s}, \quad (34)$$

and

$$F = \frac{1}{2} u_\tau H^2 \frac{\partial_{2222}\eta + 2\partial_{2233}\eta + \partial_{3333}\eta}{\partial_2\eta\partial_3u_1^s - \partial_3\eta\partial_2u_1^s}. \quad (35)$$

“Appendix B” covers use of the Faà di Bruno formula to evaluate  $n^{\text{th}}$ -order univariate and multivariate partial derivatives, as needed to compute  $A$  to  $F$  in Eqs. 30 to 35. Note also that the denominators of prefactors  $A$  to  $F$  are subjected to a mild low-pass filtering before further computation. Success of the development is not contingent upon low-pass filtering, rather this “smoothing” helps to attenuate large values that occur locally and would otherwise undermine the resultant predictions. Though brief and ostensibly solvable, we emphasize that Eq. 29 is contingent upon a priori prescription of a model for the streamfunction. This concern can be remedied, however, via prescription of a model for the mean counter-rotating cells associated with low- and high-momentum pathways and spanwise aerodynamic drag variability. Consider, for example, a streamfunction based on a single free vortex:

$$\psi(x_2, x_3; \lambda) = \alpha \exp\left(-\frac{(x_3 - \lambda/2)^4}{\alpha_{33}H^4} - \frac{(x_2 - \lambda/2)^4}{\alpha_{32}H^4}\right), \quad (36)$$

where  $\alpha$  is a circulation prefactor, and  $\alpha_{33}$  and  $\alpha_{32}$  are tuning parameters, which vary the spatial distribution of  $\psi$ , and, thus,  $\langle \omega_1 \rangle_t$ . These parameters are independently defined, in order to ensure that the resultant velocity field conforms with the boundary conditions of a turbulent wall flow. The Eq. 36 streamfunction represents a single vortex core with center-of-rotation displaced vertically at elevation,  $\lambda/2$ , and at spanwise location  $x_2 = \lambda/2$ . Any streamfunction (including the model used here) must exhibit consistency with the no-slip conditions required for a turbulent wall flow; here, this consistency can be readily assessed by consideration of the resultant velocity field spanwise-wall-normal velocity field:

$$\langle u_2 \rangle_t = \frac{\partial \psi}{\partial x_3} = -\alpha \frac{4(x_3 - \lambda/2)^3}{\alpha_{33}H^4} \exp\left(-\frac{(x_3 - \lambda/2)^4}{\alpha_{33}H^4} - \frac{(x_2 - \lambda/2)^4}{\alpha_{32}H^4}\right), \quad (37)$$

and

$$\langle u_3 \rangle_t = -\frac{\partial \psi}{\partial x_2} = \alpha \frac{4(x_2 - \lambda/2)^3}{\alpha_{32}H^4} \exp\left(-\frac{(x_3 - \lambda/2)^4}{\alpha_{33}H^4} - \frac{(x_2 - \lambda/2)^4}{\alpha_{32}H^4}\right), \quad (38)$$

where the parameters,  $\alpha_{22}$  and  $\alpha_{33}$ , force the velocities to zero (or approaching zero) at the wall and flow height. In Sect. 5, results will be shown that support this claim. The additive

nature of streamfunctions enables more complex flows to be assembled via generalization to Eq. 36, viz:

$$\begin{aligned} \psi(x_2, x_3; \lambda) = & \alpha \sum_{i=1}^{N/2} \exp \left[ -\frac{(x_3 - \frac{\lambda}{2})^4}{\alpha_{33} H^4} - \frac{(x_2 - \{2i-1\} \frac{\lambda}{2})^4}{\alpha_{32} H^2} \right] \\ & - \alpha \sum_{i=1}^{N/2} \exp \left[ -\frac{(x_3 - \frac{\lambda}{2})^4}{\alpha_{33} H^4} - \frac{(x_2 - 2i \frac{\lambda}{2})^4}{\alpha_{32} H^4} \right], \end{aligned} \quad (39)$$

where  $N$  is the number of counter-rotating vortex cores, and the summation has been decomposed into summation over odd and even indices with the first and second right-hand side terms, respectively, which enables the polarity of prefactor  $\alpha$  to vary and model counter-rotating vortex cores. Thus, if  $\alpha$  is known, the streamfunction for a range of flow regimes can be defined a priori. And since the preceding scaling analysis (Sect. 2.3) has confirmed the scaling relations for shear-normalized circulation, while Yang and Anderson [32] have revealed the amplitudes of  $\Gamma^*$ ,  $\psi(x_2, x_3; \lambda)$  can be defined. With this, we recall the initial definition of the streamfunction in Eq. 26. It follows that if  $\psi$  is known, then  $\Psi(\eta) = (Hu_\tau)^{-1} \psi$  can be evaluated using the pre-defined array of counter-rotating vortices. This leaves only  $G(x_2, x_3, \lambda, H)$  to be defined, thereby defining  $\eta$  and closing the system. The definition of  $\eta$  is constrained by the governing partial differential equation such that the any dependence upon problem parameters is consolidated within  $\eta$ . Here, we define  $G$  in a manner that captures the dependence on  $x_2, x_3, H, \lambda$ , while also simplifying computation of ordinary derivatives of  $\Psi$ . This attribute is, in fact, not necessary, but it is nonetheless helpful in the following developments. The selected model for  $G$ :

$$G(x_2, x_3, \lambda, H) = \left( \frac{(x_3 - \lambda/4)^2}{\alpha_{33} H^4} + \frac{(x_2 - \lambda/2)^4}{\alpha_{32} H^4} \right). \quad (40)$$

Though cumbersome, the partial derivatives of  $G$  can be computed with finite differences, allowing determination of prefactors  $A$  to  $F$  in Eqs. 30 to 35, respectively, thereby enabling determination of  $\langle u_1 \rangle_t$  via integration of Eq. 29 and substitution of Eq. 27.

When Eq. 40 is used for  $G(x_2, x_3, \lambda, H)$ , we can further advance Eq. 25 with  $\Psi(\eta) = \alpha^* \exp(-u_\tau/U^s \eta)$ , where  $\alpha^* = \alpha(Hu_\tau)^{-1}$ ,  $\Psi'(\eta) = -u_\tau/U^s \Psi(\eta)$ ,  $\Psi''(\eta) = (u_\tau/U^s)^2 \Psi(\eta)$ ,  $\Psi'''(\eta) = -(u_\tau/U^s)^3 \Psi(\eta)$ , and  $\Psi''''(\eta) = (u_\tau/U^s)^4 \Psi(\eta)$ , resulting in:

$$\frac{dU}{d\eta} = \left( A \left[ \frac{u_\tau}{U^s} \right]^3 - B \left[ \frac{u_\tau}{U^s} \right]^2 + C \left[ \frac{u_\tau}{U^s} \right] - D \left[ \frac{u_\tau}{U^s} \right]^2 \Psi + E \left[ \frac{u_\tau}{U^s} \right] \Psi - F \right) \left[ \frac{u_\tau}{U^s} \right] \Psi. \quad (41)$$

$\Gamma^*$  can be retrieved from a posteriori values derived from the preceding scaling analysis or from precise models derived from simulations or experiments. Integration of the Eq. 41 ordinary differential equation (ODE) yields:

$$\begin{aligned} U(\eta) = & \int_{\min(\eta)}^{\max(\eta)} \left( A \left[ \frac{u_\tau}{U^s} \right]^3 - B \left[ \frac{u_\tau}{U^s} \right]^2 + C \left[ \frac{u_\tau}{U^s} \right] - D \left[ \frac{u_\tau}{U^s} \right]^2 \Psi \right. \\ & \left. + E \left[ \frac{u_\tau}{U^s} \right] \Psi - F \right) \left[ \frac{u_\tau}{U^s} \right] \Psi d\eta, \end{aligned} \quad (42)$$

which can be evaluated with a standard numerical quadrature (we have used Reimann summation, which captures the dominant variability of Eq. 42 terms and is, thus, sufficient for the present purposes):

$$U(\eta) = \left( A \left[ \frac{u_\tau}{U^s} \right]^3 - B \left[ \frac{u_\tau}{U^s} \right]^2 + C \left[ \frac{u_\tau}{U^s} \right] - D \left[ \frac{u_\tau}{U^s} \right]^2 \Psi \right. \\ \left. + E \left[ \frac{u_\tau}{U^s} \right] \Psi - F \right) \left[ \frac{u_\tau}{U^s} \right] \Psi d\eta. \quad (43)$$

Given the functional dependence of  $\eta$  (recall Eq. 24), it is important to note that:

$$d\eta = \frac{\partial \eta}{\partial x_2} \delta x_2 + \frac{\partial \eta}{\partial x_3} \delta x_3 + \frac{\partial \eta}{\partial \lambda} \delta \lambda + \frac{\partial \eta}{\partial u_\tau} \delta u_\tau + \frac{\partial \eta}{\partial U^s} \delta U^s + \frac{\partial \eta}{\partial H} \delta H. \quad (44)$$

For presentation of results, we show  $U(\eta(x_2, x_3; \lambda, u_\tau, U^s, H))$ , and thus  $d\eta = (\partial \eta / \partial x_2) \delta x_2 + (\partial \eta / \partial x_3) \delta x_3$ . The resulting contours for  $U(\eta(x_2, x_3; \lambda, u_\tau, U^s, H))$  show the spatial variability of mean streamwise velocity for fixed values of vortex core spacing, Stokes forcing amplitude, and shear velocity. To these contours, we add a logarithmic profile, which constitutes the base state the flow would attain in the absence of spanwise topographic heterogeneity:

$$\frac{u_1^f(x_2, x_3)}{u_\tau} = \frac{1}{\kappa} \log \left( \frac{x_3}{z_0} \right) + U(\eta(x_2, x_3; \lambda, u_\tau, U^s, H)), \quad (45)$$

where  $\kappa = 0.4$  is the von Kármán constant and  $z_0/H = 10^{-4}$  is an aerodynamic roughness length. It is emphasized that the Eq. 36 streamfunction is just one of many candidate models that could have been used to represent the vortex cores. We experimented with a series of models (including an ideal vortex), and this particular model provided the most realistic input vortex cores. We emphasize, finally, that an additional test of efficacy would involve substitution of the resultant streamwise velocity (Eq. 45) and selected streamfunction (Eq. 36) back in to the original transport equation (Eq. 25), and ensuring a balance is attained. We attempted this very exercise, and attained moderate agreement between the left- and right-hand side of Eq. 25. This difficulty in balancing Eq. 25 has been well reported in other articles [31, 43].

## 4 Cases

In order to assess the efficacy of the Sect. 3 development and Eq. 45, we have selected a representative range of forcing conditions. Table 1 summarizes nine cases, presenting the tuning parameters used to model the Stokes vortex forcing (Eqs. 3 and 36). In the interest of brevity, we have not varied spacing since the present article is directed to assessment of the resultant streamwise velocity distribution (previous contributions have comprehensively addressed spacing). Instead, we have varied streamfunction amplitude,  $\alpha^*$ , and Stokes forcing amplitude,  $U^s/u_\tau$ . It is clear that Eq. 45 will tend towards a logarithmic form as these quantities approach zero (which would be analogous to reducing the height of adjacent rows of elements). Finally, the results shown in Sect. 5 are from a domain of spanwise and vertical extent,  $\{(x_2, x_3) : 0 \leq x_2/H \leq 1, 0 \leq x_3/H \leq 1\}$ , for a single vortex core of amplitude,  $\alpha^*$ . With this, we evaluate the resultant flow field,  $\langle \mathbf{u} \rangle$ , and then perform a “mirroring” of quantities about the vertical axis at  $x_2/H = 1$ , which recreates the

**Table 1** Details of surfaces and forcing conditions considered in present study

Case	$\frac{\lambda}{H}$	$\frac{U^s}{u_\tau}$	$\alpha_1$	$\alpha_2$	$\alpha_{32}$	$\alpha_{33}$	$\alpha^*$
1	1.0	0.05	0.002	0.10	0.04	0.067	0.012
2	1.0	0.05	0.002	0.10	0.04	0.067	0.020
3	1.0	0.05	0.002	0.10	0.04	0.067	0.028
4	1.0	0.10	0.002	0.10	0.04	0.067	0.012
5	1.0	0.10	0.002	0.10	0.04	0.067	0.020
6	1.0	0.10	0.002	0.10	0.04	0.067	0.028
7	1.0	0.20	0.002	0.10	0.04	0.067	0.012
8	1.0	0.20	0.002	0.10	0.04	0.067	0.020
9	1.0	0.20	0.002	0.10	0.04	0.067	0.028

presence of two counter-rotating vortices adjacent to an LMP at location  $x_2/H = 1$ . With this, the domain also includes two HMPs at locations  $x_2/H = 0$  and  $x_2/H = 2$ .

## 5 Results

For the cases summarized in Table 1, we show key first-order quantities to demonstrate efficacy of the Sect. 3 solution. Figures 2 and 3 show results for cases 1 and 8, respectively, where color flood contours of Reynolds-averaged streamwise vorticity,  $\langle \omega_1 \rangle_t H/u_\tau$ , streamwise velocity,  $\langle u_1 \rangle_t/u_\tau$ , spanwise velocity,  $\langle u_2 \rangle_t/u_\tau$ , and wall-normal velocity,  $\langle u_3 \rangle_t/u_\tau$ , is shown in Panels (a), (b), (c), and (d), respectively. The results for these cases are shown in order to consider “limiting states” within the parameter space, although the distributions are representative of intermediate states (discussion to following in text accompanying Fig. 4). The contours of  $\langle \omega_1 \rangle_t/u_\tau$  are used to demonstrate the presence of counter-rotating, secondary flows within the domain—the signature of roughness-driven turbulent secondary flows (the vector field has been added to further emphasize this point. The color flood of  $\langle u_1 \rangle_t/u_\tau$  (Panel b) further demonstrates that the similarity solution with vortex forcing yields highly realistic mean streamwise velocity distributions. For both cases, one can see a clear LMP and HMP at the locations of upwelling and downwelling, respectively. In previous articles, we have remarked that flows altered by spanwise surface heterogeneity exhibit momentum excess and deficit above the high and low roughness: a counter-intuitive outcome that can only be understood when viewed through the lens of Prandtl’s secondary flow of the second kind [31]. The analog is true here when one consults the Eq. 3 forcing condition.

Equation 3 exhibits a maximum and minimum value at  $x_2/H = 0$  ( $U^s$ ) and  $x_2/H = \lambda/H$  ( $-U^s$ ), respectively. Equation 2 presents the vortex model, where the input arguments and curl operation dictate that  $\mathbf{f}^\omega = \{0\hat{i}, -\omega_3 u_1^s \hat{j}, +\omega_2 u_1^s \hat{k}\}$ . Consider, then, the vertical components:  $f_3^\omega = \omega_2 u_1^s = \partial_3 u_1 u_1^s$ , where the vertical gradient within the equation for streamwise vorticity has been omitted owing to streamwise homogeneity of these flows [27, 31]. Since  $\partial_3 u_1$  is positive at all spanwise locations,  $f_3^\omega = \partial_3 u_1 u_1^s$  requires that the polarity of  $u_1^s$  must be positive and negative at the base of a HMP and LMP, respectively, in order to induce the downwelling and upwelling that is characteristic of these flows. Similarly, since  $f_2 = \partial_2 u_1 u_1^s$ , and because  $\partial_2 u_1 < 0$  between a HMP and LMP,  $u_1^s$  must be positive at the base of a HMP in order to induce the positive spanwise forcing associated

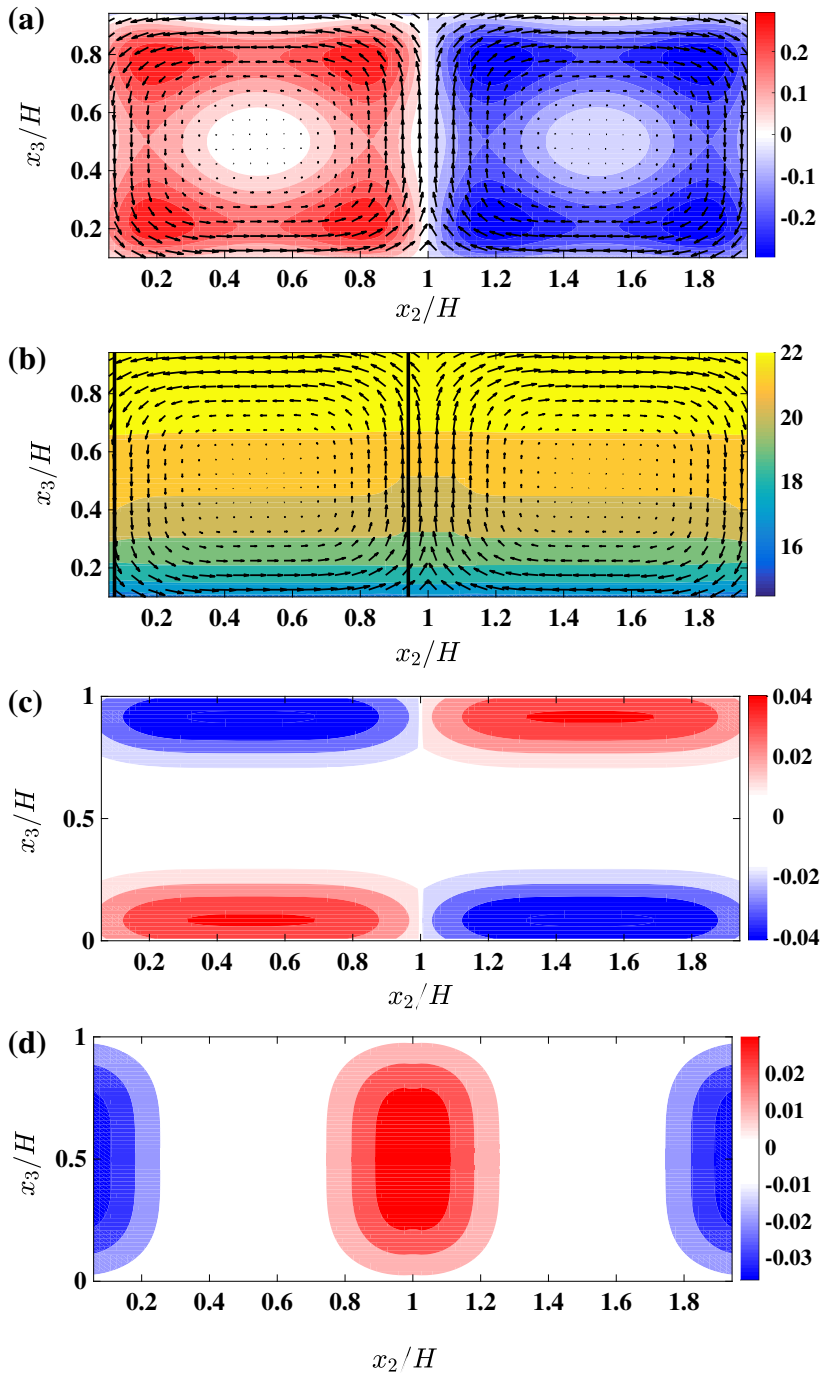


**Fig. 2** Contours of Reynolds-averaged quantities from Sect. 3, for case 1: **a**  $\langle \omega_1 \rangle_t H / u_\tau$ , **b**  $u_1^f / u_\tau$  from Eq. 45, **c**  $\langle u_2 \rangle_t / u_\tau$  and **d**  $\langle u_3 \rangle_t / u_\tau$ . On Panels (a) and (b), black vectors denote  $\{\langle u_2 \rangle_t, \langle u_3 \rangle_t\}$ . On Panel (b), vertical lines denote the locations at which Fig. 4 are retrieved

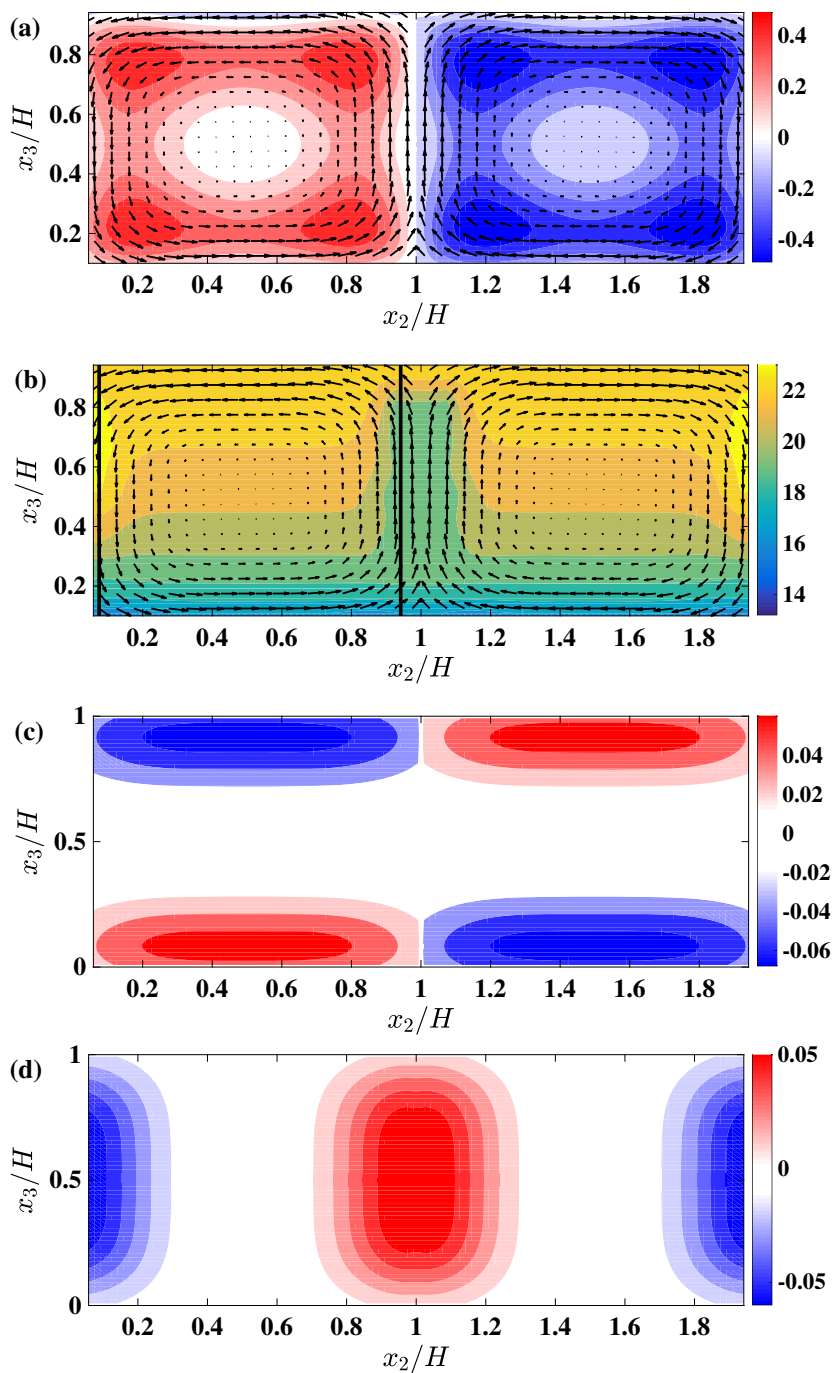


**Fig. 3** Contours of Reynolds-averaged quantities from Sect. 3, for case 8: **a**  $\langle \omega_1 \rangle_t H / u_\tau$ , **b**  $u_1' / u_\tau$  from Eq. 45, **c**  $\langle u_2 \rangle_t / u_\tau$  and **d**  $\langle u_3 \rangle_t / u_\tau$ . On Panels (a) and (b), black vectors denote  $\{ \langle u_2 \rangle_t, \langle u_3 \rangle_t \}$ . On Panel (b), vertical lines denote the locations at which Fig. 4 are retrieved

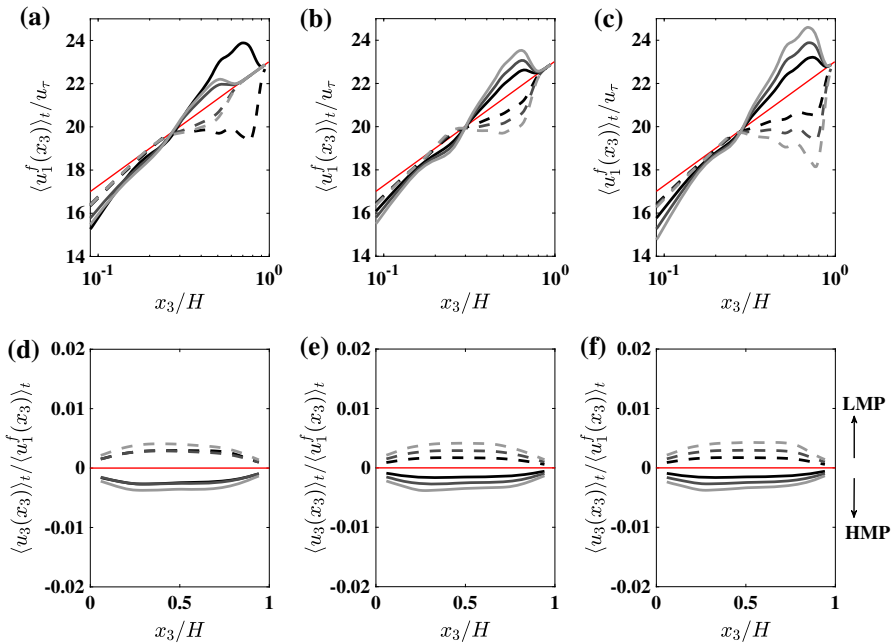


**Fig. 4** Vertical profiles of velocity components for the cases summarized in Table 1. Panels **a–c** show  $u_1^f(x_3)/u_\tau$  at spanwise locations,  $x_2/H = 0.075$  (solid lines) and  $x_2/H = 0.942$  (dashed lines); Panels **d–f** show the ratio,  $\langle u_3(x_3) \rangle_t / \langle u_1^f(x_3) \rangle_t$  at spanwise locations,  $x_2/H = 0.075$  (negative values) and  $x_2/H = 0.942$  (positive values). The spanwise locations are superimposed on Figs. 2 and 3, for perspective. Panels show: cases 1 to 3 (**a, d**), cases 4 to 6 (**b, e**), and cases 7 to 9 (**c, f**), where the first, second, and third case within each group is represented by black, intermediate gray, and light gray lines, respectively. On Panels (**a**) to (**c**), the red line represents the logarithmic streamwise velocity profile. On Panels (**d**) to (**e**), the red line represents  $\langle u_3 \rangle_t = 0$ , as would exist in a canonical channel. The HMP and LMP annotation has been added to highlight the downwelling and upwelling of fluid, respectively, owing to the counter-rotating cells

with lateral ejection of fluid at the HMP base. In summary, the Stokes model set forth here is useful but must be configured with caution, since the resultant forcing directions must be physically compliant with the choice of input streamfunction (see also Sect. 6).

The magnitude of streamwise velocity and streamwise vorticity presented in Figs. 2 and 3 is consistent with values reported from LES and experimental measurement [29, 31]. We emphasize again that the entire development is contingent upon a user-defined streamfunction and a rudimentary model for the turbulent viscosity,  $\nu_t$ . Refinements to both would potentially enhance the fidelity of the present results, although the development itself would remain identical. To this extent, we have included color flood contours for  $\langle u_2 \rangle_t / u_\tau$  and  $\langle u_3 \rangle_t / u_\tau$  on Figs. 2 and 3. As outlined in Sect. 3, Eqs. 37 and 38, these velocity components are a direct product of the a priori defined streamfunction, and we went to great lengths to ensure that the resultant velocities were consistent with a roughness-perturbed turbulent secondary flow in a channel. The figures indicate that this has been accomplished: first, Panel (c) shows a predominant “inflow” and “outflow” at the bottom and top of the LMP ( $x_2/H = 1$ ), respectively, but these zones of elevated velocity are tending toward zero at  $x_3/H = 0$ . Similarly, Panel (d) shows that  $\langle u_3 \rangle_t / u_\tau$  is zero at virtually all wall and centerline locations, with pronounced zones of upwelling and

downwelling within the LMP and HMP, respectively, which is precisely to be expected and indicative of a physically-meaningful streamfunction.

Figure 4 shows vertical profiles of streamwise and vertical velocity for all the Table 1 cases. Panels (a) to (c) show profiles within a HMP (solid profiles) and LMP (dashed profiles). The profiles are shown relative to the logarithmic base model, as per Eq. 45. Within the HMP and LMP, we observe excesses and deficits in streamwise velocity, as expected. The magnitude of diversion from the base model increases monotonically with increasing  $U^s/u_\tau$  (Panels a to c), and for increasing streamfunction amplitude. We emphasize the use of logarithmic-linear scaling, which serves to provide greater detail to the lowest 50% of the domain. We note also that the vertical gradient of  $u_1^f/u_\tau$  is markedly larger within the HMP in the region,  $0.3 \lesssim x_3/H \lesssim 0.7$ , which is entirely consistent with the notion of enhanced momentum fluxes (and drag) within HMPs, as has been shown in detail by Willingham et al. [27] and Anderson et al. [31].

Figure 4(d) to (f) show the ratio,  $\langle u_3 \rangle_t / u_1^f$ , within a HMP and LMP. It is clear that the development has captured the downwelling and upwelling that is a key attribute of these flows. Moreover, it is notable that the ratio is  $\approx 1 - 4\%$ , which compares closely with values reported in the duct flow literature [37, 39–42] and in our recent parametric study [32]. We note, again, that the profiles vary monotonically, and that enhanced forcing results in more vigorous downwelling and upwelling. In the following section, results are shown from a series of LES cases wherein the Eq. 3 vortex forcing parameters are varied to capture roughness and topography cases [32]. Section 6 culminates in showing that the ratio,  $\langle u_3 \rangle_t / u_1^f$ , exhibits trends and magnitudes closely resembling those derived from the present similarity solution.

## 6 Large-eddy simulation with vortex forcing model

In order to demonstrate efficacy of Eq. 3, and thus the subsequent developments in Sects. 2 and 3, we have performed a series of large-eddy simulation (LES) cases. We consider flow over surfaces with a homogeneous roughness distribution, with attributes summarized in Table 2. During LES, the spatially-filtered, three-dimensional incompressible momentum transport equations are solved at high-Reynolds number [60, 61] for a neutrally-stratified (i.e. no buoyancy forces) turbulent channel flow:

**Table 2** Details of LES cases and vortex forcing model parameters for Sect. 6

Case	$\frac{2\lambda}{H}$	$\frac{U^s}{u_\tau}$	$\alpha_1$	$\alpha_2$	$L_1/H$	$L_2/H$	$N_1 \times N_2 \times N_3$
L1	0.2	0.02	0.002	0.100	3.2	3.2	$128 \times 128 \times 128$
L2	0.8	0.02	0.002	0.100	3.2	3.2	$128 \times 128 \times 128$
L3	1.6	0.20	0.002	0.100	3.2	3.2	$128 \times 128 \times 128$
L4	3.2	0.20	0.002	0.100	3.2	3.2	$128 \times 128 \times 128$
L5	2.0	0.20	0.002	0.100	2.0	2.0	$128 \times 128 \times 128$
L6	2.0	0.67	0.002	0.100	2.0	2.0	$128 \times 128 \times 128$

$$\frac{\partial \tilde{\mathbf{u}}}{\partial t} + \frac{1}{2} \nabla (\tilde{\mathbf{u}} \cdot \tilde{\mathbf{u}}) - \tilde{\mathbf{u}} \times \tilde{\boldsymbol{\omega}} = -\frac{1}{\rho} \nabla \tilde{p} - \nabla \cdot \boldsymbol{\tau} + \boldsymbol{\Pi} + \frac{1}{\rho} \mathbf{f}^w, \quad (46)$$

where  $\tilde{p}$  is the modified pressure,  $\boldsymbol{\tau} = \widetilde{\mathbf{u} \otimes \mathbf{u}} - \tilde{\mathbf{u}} \otimes \tilde{\mathbf{u}}$  is the subgrid-scale (SGS) stress tensor, and  $\boldsymbol{\Pi} = \{u_\tau^2/H, 0, 0\}$  is an imposed mean pressure gradient in the streamwise direction, where  $u_\tau$  is the shear velocity and  $H$  is a predefined channel half height. Note that Eqs. 1 and 46 are the Reynolds- and spatially-averaged version of the momentum transport equation, where a spatially-filtered quantity is denoted by  $\tilde{\cdot}$ , and is the product of convolution with a filtering kernel with grid-filter scale resolution, i.e.,  $\tilde{\mathbf{u}}(\mathbf{x}, t) = G_\Delta \star \mathbf{u}(\mathbf{x}, t)$ . A solenoidal velocity field is maintained by computing the divergence of Eq. 46, applying the incompressibility condition,  $\nabla \cdot \tilde{\mathbf{u}} = 0$ , and solving the resulting pressure Poisson equation for a pressure correction. Note also that the viscous stresses,  $\nu \nabla^2 \tilde{\mathbf{u}}$ , are omitted from Eq. 46, owing to the high-Reynolds number “fully rough” conditions typical of ambient conditions in engineering and geophysical flows (the ‘macroscale’ Reynolds number is  $Re_\tau = u_\tau H / \nu \sim \mathcal{O}(10^7)$ ) [62]. The deviatoric component of  $\boldsymbol{\tau}$  is evaluated using the eddy-viscosity modeling approach,

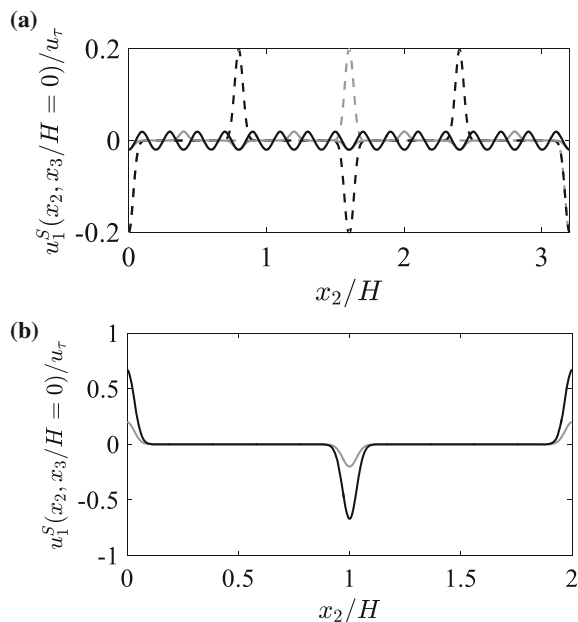
$$\boldsymbol{\tau} - \frac{1}{3} \delta \text{Tr}(\boldsymbol{\tau}) = -2\nu_t \tilde{\mathbf{S}} \quad (47)$$

where  $\nu_t = (C_s \Delta)^2 |\tilde{\mathbf{S}}|$  is the turbulent viscosity,  $C_s$  is the Smagorinsky coefficient,  $\Delta$  is the filter size,  $\tilde{\mathbf{S}} = \frac{1}{2} (\nabla \tilde{\mathbf{u}} + \nabla \tilde{\mathbf{u}}^T)$  is the resolved strain-rate tensor, and  $|\tilde{\mathbf{S}}| = (2\tilde{\mathbf{S}} : \tilde{\mathbf{S}})^{1/2}$  is magnitude of the resolved strain-rate tensor. For this work,  $C_s$  is evaluated dynamically during LES with the Lagrangian scale-dependent dynamic SGS model [63]. Pseudospectral discretization is used in the horizontal directions, while vertical gradients are evaluated with centered second-order finite differencing. Periodic boundary conditions are imposed on the vertical planes of the domain, owing to spectral discretization in the horizontal directions. At the domain top, the zero-stress Neumann boundary condition is imposed on streamwise and spanwise velocity,  $\partial \tilde{u}_1 / \partial x_3|_{x_3/H=0} = \partial \tilde{u}_2 / \partial x_3|_{x_3/H=0} = 0$ . The zero vertical velocity condition is imposed at the domain top and bottom,  $\tilde{u}_3(x_1, x_2, x_3/H=0) = \tilde{u}_3(x_1, x_2, x_3/H=1) = 0$ . Zero-stress Neumann boundary conditions are imposed on the pressure Poisson equation solution at the domain top and bottom,  $\partial \tilde{p} / \partial x_3|_{x_3/H=0} = \partial \tilde{p} / \partial x_3|_{x_3/H=1} = 0$ . The Adams-Bashforth time-advancement scheme is used for temporal integration of Eq. 1. The nonlinear advection term is de-aliased in Fourier space with the 3/2 rule [64]; this is necessary since aliasing errors may contaminate the smallest resolved scales of the flow, compromising predictions of the SGS models. Table 2 summarizes the simulation attributes, where  $L_1/H$  and  $L_2/H$  is the domain streamwise and spanwise extent, respectively. The computational domain is staggered in the vertical direction; the first computational level for  $\tilde{u}_1$  and  $\tilde{u}_2$  is located at elevation  $\frac{1}{2} \delta x_3$ .

For studying wall turbulence responding to spanwise surface heterogeneity, the vortex forcing model is compelling since one need only define the Eq. 3 function during LES, where the parameters are selected to capture different values of spacing. Moreover, the amplitude,  $U_s/u_\tau$ , is a proxy for roughness element height,  $h/H$ . In order to implement the vortex forcing,  $\mathbf{u}^s = \{u_1^s, u_2^s, u_3^s\} = \{u_1^s, 0, 0\}$  is defined a priori, and then  $\mathbf{f}^w = \tilde{\boldsymbol{\omega}} \times \mathbf{u}^s = \{0, -u_1^s \tilde{\omega}_3, u_1^s \tilde{\omega}_2\}$  is computed during simulation (i.e., instantaneous version of Eq. 2). Figure 5a, b show profiles of the streamwise component of Eq. 3 for cases L1–L4 and L5 and L6, respectively; see also Table 2 for a summary of vortex forcing model parameters.

**Fig. 5** Profiles of the streamwise component of Eq. 3 at elevation,  $x_3/H = 0$ , where

$\mathbf{u}^s = \{u_1^s, u_2^s, u_3^s\} = \{u_1^s, 0, 0\}$ . Panels **a** and **b** shows cases L1–L4 and L5 and L6, respectively. On Panel (a), profiles correspond with L1 (solid black), L2 (solid gray), L3 (dashed black), and L4 (dashed gray). On Panel (b), profiles correspond with L5 (solid black) and L6 (solid gray)



These cases were selected based on the findings from Yang and Anderson [32], wherein the surface behaves as a roughness or topography for  $2\lambda < H$  or  $2\lambda > 2H$ , respectively. Users then define a surface stress at the lower boundary, where the equilibrium logarithmic law is conventionally used for these turbulent channel flows [60, 65, 66]:

$$\frac{\tau_{i3}^w(x_1, x_2, \delta x_3/2)}{\rho} = - \left[ \frac{\kappa U(x_1, x_2, \delta x_3/2)}{\log(\frac{1}{2} \delta x_3/z_0)} \right]^2 \frac{\widehat{u}_i(x_1, x_2, \delta x_3/2)}{U(x_1, x_2, \delta x_3/2)}, \quad (48)$$

where  $i = 1$  and  $2$ ,  $\kappa$  is the von Kármán constant ( $\kappa = 0.4$ ),  $\widehat{\dots}$  denotes test filtering, and  $U(x_1, x_2, \delta x_3/2) = \left[ \widehat{u}_1^2(x_1, x_2, \delta x_3/2) + \widehat{u}_2^2(x_1, x_2, \delta x_3/2) \right]^{1/2}$  is magnitude of the local test-filtered velocity. We follow Bou-Zeid et al. [63] by using the test-filtered velocities for computing the wallstress (Eq. 48). In the present study, we used  $z_0/H = 10^{-5}$ .

## 6.1 Results

Here, we provide instantaneous and Reynolds-averaged results that demonstrate how turbulent channel flow over a homogeneous roughness (Eq. 48) responds to the addition of a vortex forcing term (Eq. 46, Fig. 5, and accompanying text in Sect. 6). The results are shown for the cases summarized in Table 2. Figure 6 shows instantaneous flow visualization in the spanwise–wall-normal plane, where signed swirl strength,  $\lambda_{ci}\widehat{\omega}_1/|\widehat{\omega}|$  [67], is used to highlight regions of rotation. For cases L1 and L2, for which the surface is rendered a roughness by virtue of the small spanwise spacing (Table 2), the flow field does not exhibit a distinct connection to the vortex forcing. This result is entirely consistent with observations of Yang and Anderson [32], who showed that when the spanwise spacing between rows of adjacent roughness elements is “small”—for example, 10–30% of the flow depth—topographic disturbances are confined to the roughness sublayer.

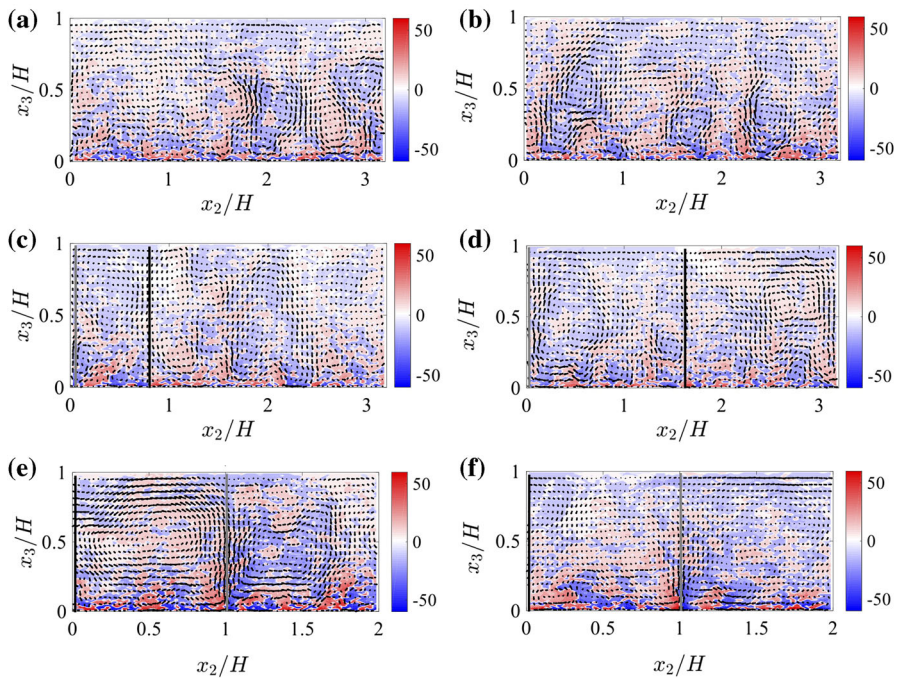


**Fig. 6** Spanwise–wall-normal contours of instantaneous swirl strength signed by instantaneous streamwise vorticity,  $\lambda_{ci}\tilde{\omega}_1/|\tilde{\omega}|$  [67], with vectors of instantaneous spanwise and vertical velocity,  $\{\tilde{u}_2, \tilde{u}_3\}$ , superimposed. Panels correspond with cases L1 (a), L2 (b), L3 (c), L4 (d), L5 (e), and L6 (f). Location of HMP and LMP denoted by vertical solid black and solid gray lines, respectively (these profiles are excluded for Panels a and b, since the spacing is so small that a HMP or LMP is unable to form). See Fig. 5 for graphical illustration of vortex forcing model input profiles

For case L3 and L4, however, even the instantaneous data shows the signature of the vortex forcing model, with zones of positive and negative  $\lambda_{ci}\tilde{\omega}_1/|\tilde{\omega}|$  in regions that flank cites of prominent downwelling and upwelling (evident from inspection of the vector field). From Fig. 5 and the preceding theoretical developments in Sects. 2 and 3, it was established that downwelling and upwelling occurs above maxima and minima in  $u_1^s$ , respectively. With this, the instantaneous case L3 result (Fig. 6c) shows upwelling at  $x_2/H \approx 0$ ,  $\approx 1.6$ , and  $\approx 3.2$ , and downwelling at  $x_2/H \approx 0.8$  and  $\approx 2.4$  (consistent with forcing, as shown by Fig. 5). Similar consistency is evident for cases S4, S5, and S6, in Fig. 6d, e, f, respectively, thereby confirming efficacy of the vortex forcing approach for the present simulations.

Figure 7 shows Reynolds-averaged flow quantities in the spanwise–wall-normal plane for the cases summarized in Table 2. The figure format is identical to Fig. 6, except that we now show Reynolds-averaged quantities. It is clear, firstly, that for cases L1 and L2 (Fig. 7a,b) the high-magnitude flow disturbances are concentrated in the roughness sub-layer, and this attenuates rapidly in the wall-normal direction. Again, this result is thoroughly consistent with our preceding efforts, in which the flow was physically perturbed with obstacles that were resolved with an immersed boundary method [32] (note that for Figs. 6 and 7, equivalent colourbar limits were used when generating the colour flood contours, which helps to objectively compare between cases).

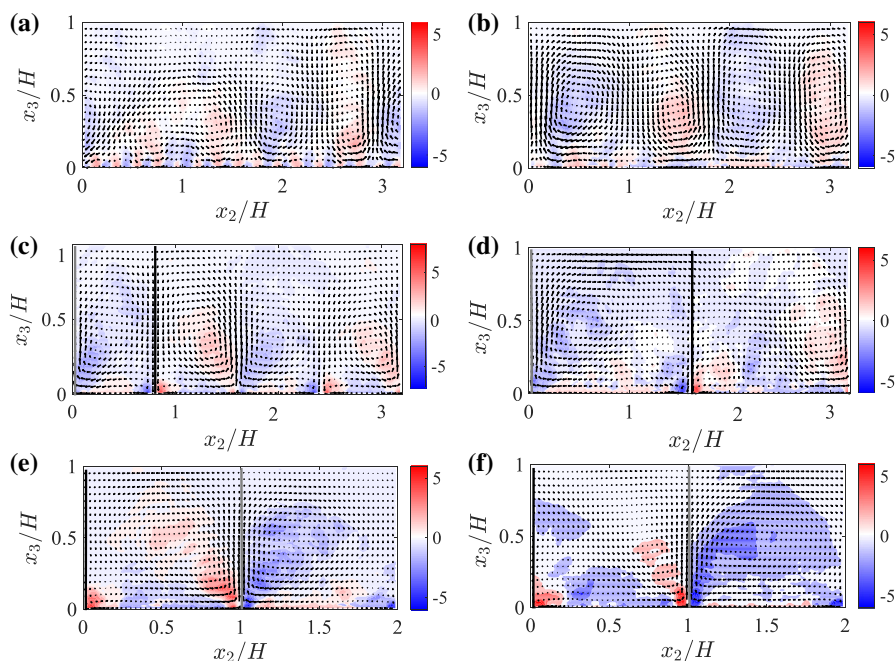
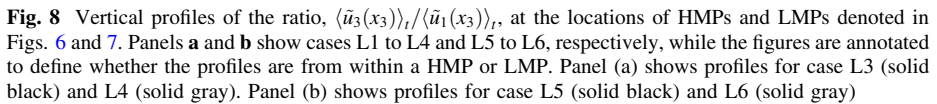


**Fig. 7** Spanwise–wall-normal contours of Reynolds-averaged swirl strength signed by Reynolds-averaged streamwise vorticity,  $\langle \lambda_{ci} \rangle_t \langle \tilde{\omega}_1 \rangle_t / |\langle \tilde{\omega} \rangle_t|$  [67], with vectors of Reynolds-averaged spanwise and vertical velocity,  $\{\langle \tilde{u}_2 \rangle_t, \langle \tilde{u}_3 \rangle_t\}$ , superimposed. Panels correspond with cases L1 (a), L2 (b), L3 (c), L4 (d), L5 (e), and L6 (f). Location of HMP and LMP denoted by vertical solid black and solid gray lines, respectively (these profiles are excluded for Panels a and b, since the spacing is so small that a HMP or LMP is unable to form). See Fig. 5 for graphical illustration of vortex forcing model input profiles

For cases L3 and L4, larger spacing allows the rollers to grow in spatial extent, while the magnitude of  $\langle \lambda_{ci} \rangle_t \langle \tilde{\omega}_1 \rangle_t / |\langle \tilde{\omega} \rangle_t|$  is roughly equal between the cases since the prefactor,  $U_s/u_\tau$ , is equivalent. For the cases in which a smaller domain is used, the spatial patterns are entirely consistent with central upwelling at the domain center. However, the magnitude of  $\langle \lambda_{ci} \rangle_t \langle \tilde{\omega}_1 \rangle_t / |\langle \tilde{\omega} \rangle_t|$  for case L6 is roughly three times that for case L5. Note, however, that the vortex forcing model prefactor,  $U_s/u_\tau$ , differs by roughly the same amount (see Table 2). It is important to stress that consideration of cases L5 and L6, for which the computational domain spatial extent is smaller than for cases L1 to L4, demonstrates that grid resolution is not a control on application of the vortex forcing model. The results presented here are compelling for two reasons: (1) they confirm efficacy of the preceding scaling analysis and similarity solution (Sects. 2 and 3, respectively); and (2) they confirm that a vortex forcing model can be used to impart realistic properties of wall turbulence when perturbed by spanwise heterogeneity.

On Figs. 6 and 7, Panels (c) to (f), we included vertical lines denoting LMPs (gray) and HMPs (black), respectively, conceptually identical to the annotations on Figs. 2b and 3b. The lines graphically represent the data used to generate vertical profiles of the ratio,  $\langle \tilde{u}_3 \rangle_t / \langle \tilde{u}_1 \rangle_t$ , in order to provide an additional test of model efficacy and to compare with the similarity solution result in Sect. 3, Fig. 4d to f. For cases L3 to L6, vertical profiles of the ratio are shown in Fig. 8, where the annotations denote whether the profiles were derived from within an LMP or HMP (profiles for cases L1 and L2 are excluded since the ratio was



The profiles for cases L3 and L4 (Fig. 5a) are virtually indistinguishable, which is to be expected since the vortex forcing amplitude was equivalent (Table 2) and the spacing is sufficiently large to allow domain-scale turbulent secondary flows (Fig. 7c,d). Moreover, note that for these cases, the magnitude of the ratio compares favorably against the profiles in Fig. 4. Since  $U_s/u_\tau = 0.2$  for cases L3, L4, and L5, the resultant  $\langle \tilde{u}_3(x_3) \rangle_t / \langle \tilde{u}_1(x_3) \rangle_t$  profiles should be roughly equivalent for these cases (even with different domain sizes): Fig. 8b confirms that this is roughly true (some deviations are to be expected and can be attributed to difficulties in attain truly Reynolds-averaged data from a single profile). However, for case L6,  $\langle \tilde{u}_3(x_3) \rangle_t / \langle \tilde{u}_1(x_3) \rangle_t$  is substantially larger, owing to the much larger amplitude.

## 7 Conclusion

A series of theoretical developments have been used to deduce the scaling arguments for circulation intensity, with the results comparing favorably against results from a recent parametric study [32]. With this, the authors recast the Reynolds-averaged streamwise vorticity transport equation—subjected to a vortex forcing based upon the well-known Stokes profile—in a similarity form by virtue of an introduced similarity variable. The subsequent development yields a prognostic model for streamwise velocity that exhibits spatial trends and magnitudes in agreement with published data from experiments and simulations. The development is contingent upon a priori prescription of a turbulent vorticity and streamfunction, where, for expedience, the former was set to the product of shear velocity and flow depth, while the latter was prescribed based on antecedent results from simulations and experiments. We were entirely transparent about this attribute of the similarity solution, and presented candidate values that enabled solution. Of course, further generalizations are possible, although these are not expected to materially change the nature of the similarity solution.

The scaling analysis and similarity solution were contingent upon application of a vortex forcing model. In order to demonstrate efficacy of this model, a suite of LES cases were considered wherein the grid-filtered momentum transport equation was forced with the vortex forcing model, with input parameters varied to replicate conditions of the similarity solution. For small spacing cases, spanwise “topographic” heterogeneity effects are confined to the roughness sublayer, while Reynolds-averaged domain-scale counter-rotating rolls emerge as the spacing is increased to larger values. The results do not display any sensitivity to grid resolution, and are entirely consistent with comparable simulations when the secondary flows are forced by actual topographic elements. Thus, the article presents a forcing scheme that may find utility in flows responding to some spanwise heterogeneity, and a prognostic tool for such flows. We consider open-channel flows in river hydraulics to be one such example [24, 26, 36], where the presence of spanwise-varying surface roughness—for example, adjacent patches of fine gravel and low-height vegetation—is common.

**Acknowledgements** This work was supported by the U.S. Air Force Office of Scientific Research, Grant # FA9550-14-1-0394 (WA, JY) and Grant # FA9550-14-1-0101 (WA, AA), and by the Texas General Land Office, Contract # 16-019-0009283 (WA, KS).

## Appendix A: Datapoints from Yang and Anderson (2017)

Figure 1 showed datapoints of compensated circulation from Yang and Anderson [32]. For that study, LES with an IBM was used to model flow over a series of topographies composed of streamwise-aligned, vertically-truncated pyramid obstacles. For the simulations, we used the LES code already described in Sect. 6 (while the IBM has been outlined in many previous articles [68]). Figure 9a shows a sample arrangement, while Fig. 9b is a close-up sketch of the elements. Two sets of simulations were considered: (a) Set 1 featured elements with  $H/h = 15$ ; (b) Set 2 featured elements with  $H/h = 20$ .

For Set 1, we considered  $s_2/H = \{0.1, 0.2, 0.32, 0.46, 0.53, 0.64, 0.8, 1.0, \frac{1}{2}\pi, 2\pi\}$ , while for Set 2 we considered  $s_2/H = \{0.32, 0.46, 0.64, 1.0, \pi, 2\pi\}$ . Figure 9b shows detailed attributes of the elements; for all cases,  $w_b/H = 0.0756$ ,  $l_b/H = 0.0756$ ,  $w_t/H = 0.025$ ,  $l_t/H = 0.025$ , and  $s_x/H = 0.0756$ . For Set 1 and Set 2,  $\theta = 69.30$  and

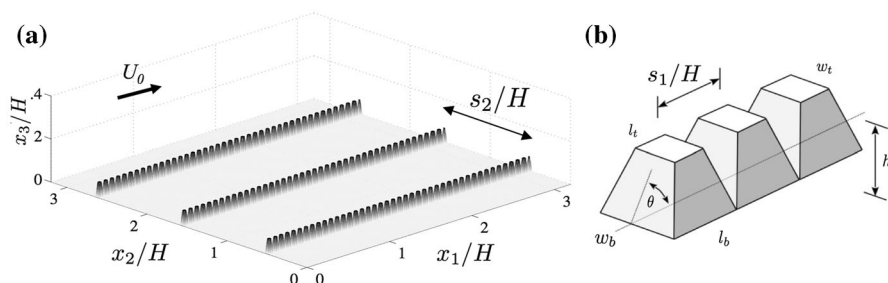


**Fig. 9** Illustration of spanwise heterogeneous topography composed of streamwise-aligned rows of pyramidal obstacles: **a** perspective image showing spacing between adjacent rows,  $s_2/H$ , and obstacle height,  $h/H$  and **b** close up of obstacles showing streamwise spacing,  $s_1$ , inclination,  $\theta$ , width and length at base,  $w_b$  and  $w_t$ , respectively, and width and length at top,  $w_t$  and  $l_t$ , respectively. Pressure-gradient forcing aligned with  $x_1$  direction, as shown with  $U_0$ . In figure, all lengths normalized by channel half height,  $H$

58.52, respectively, though we stress that  $\theta$  is not expected to have a material affect on conclusions of this study, given the fully rough flow conditions [2, 69].

## Appendix B: Faá di Bruno Formula

The univariate Faá di Bruno formula:

$$\frac{\partial^n g(f(x))}{\partial x} = \sum \frac{n!}{b_1!b_2!\dots b_n!} g^{(k)}(f(x)) \prod_{j=1}^n \left( \frac{f^{(j)}(x)}{j!} \right)^{b_j}, \quad (49)$$

where the summation is over all possible solutions with non-negative integer input arguments to the relations,  $b_1 + 2b_2 + \dots + nb_n = n$  and  $k = \sum_{i=1}^n b_i$ . With this, the first-order derivatives in  $x_2$  and  $x_3$  are:

$$\partial_2 \Psi = \Psi' \partial_2 \eta, \quad (50)$$

and

$$\partial_3 \Psi = \Psi' \partial_3 \eta, \quad (51)$$

where the summation is made over a single partition: (1)  $b_1 = 1$ , and  $k = 1$ . The second-order derivatives in  $x_2$  and  $x_3$  are:

$$\partial_{22} \Psi = \Psi'' [\partial_2 \eta]^2 + \Psi' \partial_{22} \eta, \quad (52)$$

and

$$\partial_{33} \Psi = \Psi'' [\partial_3 \eta]^2 + \Psi' \partial_{33} \eta, \quad (53)$$

where the summation is made over two partitions: (1)  $b_1 = 2$ ,  $b_2 = 0$ , and  $k = 2$ ; and (2)  $b_1 = 0$ ,  $b_2 = 1$ , and  $k = 1$ . The third-order derivatives in  $x_2$  and  $x_3$  are:

$$\partial_{222} \Psi = \Psi''' [\partial_2 \eta]^3 + 3\Psi'' \partial_2 \eta \partial_{22} \eta + \Psi' \partial_{222} \eta, \quad (54)$$

and

$$\partial_{333} \Psi = \Psi''' [\partial_3 \eta]^3 + 3\Psi'' \partial_3 \eta \partial_{33} \eta + \Psi' \partial_{333} \eta, \quad (55)$$

where the summation is made over three partitions: (1)  $b_1 = 3$ ,  $b_2 = 0$ ,  $b_3 = 0$ , and  $k = 3$ ; (2)  $b_1 = 0$ ,  $b_2 = 0$ ,  $b_3 = 1$ , and  $k = 1$ ; and (3)  $b_1 = 1$ ,  $b_2 = 1$ ,  $b_3 = 0$ , and  $k = 2$ . The fourth-order derivatives in  $x_2$  and  $x_3$  are:

$$\partial_{2222} \Psi = \Psi'''' [\partial_2 \eta]^4 + 6\Psi''' [\partial_2 \eta]^2 \partial_{22} \eta + 4\Psi'' \partial_2 \eta \partial_{222} \eta + \Psi' \partial_{2222} \eta, \quad (56)$$

and

$$\partial_{3333} \Psi = \Psi'''' [\partial_3 \eta]^4 + 6\Psi''' [\partial_3 \eta]^2 \partial_{33} \eta + 4\Psi'' \partial_3 \eta \partial_{333} \eta + \Psi' \partial_{3333} \eta, \quad (57)$$

where the summation is made over four partitions: (1)  $b_1 = 4$ ,  $b_2 = 0$ ,  $b_3 = 0$ ,  $b_4 = 0$ , and  $k = 4$ ; (2)  $b_1 = 0$ ,  $b_2 = 0$ ,  $b_3 = 0$ ,  $b_4 = 1$ , and  $k = 1$ ; (3)  $b_1 = 1$ ,  $b_2 = 0$ ,  $b_3 = 1$ ,  $b_4 = 0$ , and  $k = 2$ ; and (4)  $b_1 = 2$ ,  $b_2 = 1$ ,  $b_3 = 0$ ,  $b_4 = 0$ , and  $k = 3$ . Finally, a multivariate version of Eq. 49 is needed for terms in Eq. 25. The multivariate form of Eq. 49 yields,

$$\partial_{223}\Psi = \Psi''''[\partial_2\eta]^2\partial_3\eta + \Psi''\left[\partial_3(\partial_2\eta)^2 + \partial_{22}\eta\partial_3\eta\right] + \Psi'\partial_{223}\eta, \quad (58)$$

$$\partial_{332}\Psi = \Psi''''[\partial_3\eta]^2\partial_2\eta + \Psi''\left[\partial_2(\partial_3\eta)^2 + \partial_{33}\eta\partial_2\eta\right] + \Psi'\partial_{332}\eta, \quad (59)$$

and

$$\begin{aligned} \partial_{3322}\Psi = & \Psi''''[\partial_2\eta]^2[\partial_3\eta]^2 + \Psi''''\left(2\partial_2\eta\partial_2[\partial_3\eta]^2 + \partial_{22}\eta[\partial_3\eta]^2 + \partial_{33}\eta[\partial_2\eta]^2\right) \\ & + \Psi''\left(2\left[\partial_{23}\eta\right]^2 + \partial_3\eta\partial_{223}\eta + \partial_2\eta\partial_{332}\eta\right) + \partial_{22}\eta\partial_{332}\eta + \partial_{2233}\eta\Psi', \end{aligned} \quad (60)$$

where it has been presumed throughout that the partial differential operators commute. Note that the efficacy of Eqs. 58 and 59 can be quickly established by setting index 3 to 2 or setting index 2 to 3 in the former and latter, respectively, and comparing against Eqs. 54 and 55. In addition, the denominators of prefactors A to F (Eqs. 30 to 35) make use of the spatial derivatives of the Eq. 3 Stokes drift function, which are defined here for completeness:

$$\partial_3 u_1^s = -U^s \frac{2x_3}{\alpha_2 H^2} \left( \exp\left[-\frac{x_2^2}{\alpha_1 H^2}\right] - \exp\left[-\frac{\{x_2 - \lambda\}^2}{\alpha_1 H^2}\right] \right) \exp\left(-\frac{x_3^2}{\alpha_2 H^2}\right), \quad (61)$$

and,

$$\partial_2 u_1^s = U^s \frac{2}{\alpha_1 H^2} \left( \{x_2 - \lambda\} \exp\left[-\frac{\{x_2 - \lambda\}^2}{\alpha_1 H^2}\right] - x_2 \exp\left[-\frac{x_2^2}{\alpha_1 H^2}\right] \right) \exp\left(-\frac{x_3^2}{\alpha_2 H^2}\right). \quad (62)$$

## References

1. Raupach M, Antonia R, Rajagopalan S (1991) Rough-wall turbulent boundary layers. *Appl Mech Rev* 44:1
2. Jimenez J (2004) Turbulent flow over rough wall. *Annu Rev Fluid Mech* 36:173
3. Castro I (2007) Rough-wall boundary layers: mean flow universality. *J Fluid Mech* 585:469
4. Grass A (1971) Structural features of turbulent flow over smooth and rough boundaries. *J Fluid Mech* 50:233
5. Ghisalberti M (2009) Obstructed shear flows: similarities across systems and scales. *J Fluid Mech* 641:51
6. Anderson W, Li Q, Bou-Zeid E (2015) Numerical simulation of flow over urban-like topographies and evaluation of turbulence temporal attributes. *J Turbul* 16(9):809
7. Pan Y, Chamecki M (2016) A scaling law for the shear-production range of second-order structure functions. *J Fluid Mech* 801:459
8. Marusic I, Mathis R, Hutchins N (2010) Predictive model for wall-bounded turbulent flow. *Science* 329:193
9. Mathis R, Hutchins N, Marusic I (2009) Large-scale amplitude modulation of the small-scale structures in turbulent boundary layers. *J Fluid Mech* 628:311
10. Anderson W (2016) Conditionally averaged large-scale motions in the neutral atmospheric boundary layer: insights for Aeolian processes. *J Fluid Mech* 789:567
11. Townsend A (1976) The structure of turbulent shear flow. Cambridge University Press, Cambridge
12. Volino R, Schultz M, Flack K (2007) Turbulence structure in rough- and smooth-wall boundary layers. *J Fluid Mech* 592:263
13. Alfredsson P, Örlu R (2010) The diagnostic plot-a litmus test for wall-bounded turbulence data. *Eur J Mech B Fluids* 29:403

14. Wu Y, Christensen KT (2010) Spatial structure of a turbulent boundary layer with irregular surface roughness. *J Fluid Mech* 655:380
15. Alfredsson P, Segalini A, Örlu R (2011) A new scaling for the streamwise turbulence intensity in wall-bounded turbulent flows and what it tells us about the “outer” peak. *Phys Fluids* 23:702
16. Hong J, Katz J, Meneveau C, Schultz M (2012) Coherent structures and associated subgrid-scale energy transfer in a rough-wall channel flow. *J Fluid Mech* 712:92
17. Bou-Zeid E, Meneveau C, Parlange M (2004) Large-eddy simulation of neutral atmospheric boundary layer flow over heterogeneous surfaces: Blending height and effective surface roughness. *Water Resour Res* 40:W02505
18. Yang X (2016) On the mean flow behaviour in the presence of regional-scale surface roughness heterogeneity. *Bound-Layer Met* 161:127
19. Macdonald R, Griffiths R, Hall D (1998) An improved method for the estimation of surface roughness of obstacle arrays. *Atmospheric Environment* 32(11):1857
20. Wood D (1981) The growth of internal layer following a step change in surface roughness. Report T.N. – FM 57, Dept. of Mech. Eng., Univ. of Newcastle, Australia
21. Andreopoulos J, Wood D (1982) The response of a turbulent boundary layer to a short length of surface roughness. *J Fluid Mech* 118:143
22. Antonia R, Luxton R (1971) The response of a turbulent boundary layer to a step change in surface roughness Part I. Smooth to rough. *J Fluid Mech* 48:721
23. Garratt J (1990) The internal boundary layer: a review. *Bound-Layer Meteorol* 40:171
24. Wang ZQ, Cheng NS (2005) Secondary flows over artificial bed strips. *Adv. Water Resour* 28:441
25. Mejia-Alvarez R, Christensen K (2013) Wall-parallel stereo PIV measurements in the roughness sub-layer of turbulent flow overlying highly-irregular roughness. *Phys Fluids* 25:115109
26. Vermaas D, Uijttewall W, Houtink A (2011) Lateral transfer of streamwise momentum caused by a roughness transition across a shallow channel. *Water Resour Res* 47:W02530
27. Willingham D, Anderson W, Christensen KT, Barros J (2013) Turbulent boundary layer flow over transverse aerodynamic roughness transitions: induced mixing and flow characterization. *Phys Fluids* 26:025111
28. Nugroho B, Hutchins N, Monty J (2013) Large-scale spanwise periodicity in a turbulent boundary layer induced by highly ordered and direction surface roughness. *Int J Heat Fluid Flow* 41:90
29. Barros J, Christensen K (2014) Observations of turbulent secondary flows in a rough-wall boundary layer. *J Fluid Mech* 748:1
30. Vanderwel C, Ganapathisubramani B (2015) Effects of spanwise spacing on large-scale secondary flows in rough-wall turbulent boundary layers. *J. Fluid Mech.* <https://doi.org/10.1017/jfm.2015.292>
31. Anderson W, Barros J, Christensen K, Awasthi A (2015) Numerical and experimental study of mechanisms responsible for turbulent secondary flows in boundary layer flows over spanwise heterogeneous roughness. *J Fluid Mech* 768:316
32. Yang J, Anderson W (2017) Turbulent channel flow over surfaces with variable spanwise heterogeneity: establishing conditions for outer-layer similarity. *Flow Turbul Combust.* <https://doi.org/10.1007/s10494-017-9839-5>
33. Medjnoun T, Vanderwel C, Ganapathisubramani B (2018) Characteristics of turbulent boundary layers over smooth surfaces with spanwise heterogeneities. *J Fluid Mech* 838:516
34. Awasthi A, Anderson W (2018) Numerical study of turbulent channel flow perturbed by spanwise topographic heterogeneity: amplitude and frequency modulation within low-and high-momentum pathways. *Phys Rev Fluids* 3:044602
35. Bou-Zeid E, Parlange M, Meneveau C (2007) On the parameterization of surface roughness at regional scales. *J Atmos Sci* 64:216
36. Nezu I, Nakagawa H (1993) *Turbulence in open-channel flows*. Balkema Publishers, Rotterdam
37. Prandtl L (1952) *Essentials of fluid dynamics*. Blackie and Son, London
38. Hoagland L (1960) Fully developed turbulent flow in straight rectangular ducts—secondary flow, its cause and effect on the primary flow. Ph.D. thesis, Massachusetts Inst. of Tech
39. Brundrett E, Baines WD (1964) The production and diffusion of vorticity in duct flow. *J Fluid Mech* 19:375
40. Perkins H (1970) The formation of streamwise vorticity in turbulent flow. *J Fluid Mech* 44:721
41. Gessner F (1973) The origin of secondary flow in turbulent flow along a corner. *J Fluid Mech* 58:1
42. Bradshaw P (1987) Turbulent secondary flows. *Ann Rev Fluid Mech* 19:53
43. Madabhushi R, Vanka S (1991) Large eddy simulation of turbulence-driven secondary flow in a square duct. *Phys Fluids A* 3:2734
44. Leibovich S (1977) Convective instability of stably stratified water in the ocean. *J Fluid Mech* 82:561

45. Leibovich S (1980) On wave-current interaction theories of Langmuir circulations. *J Fluid Mech* 99:715724
46. Leibovich S (1983) The form and dynamics of Langmuir circulation. *Annu Rev Fluid Mech* 15:391
47. Craik A (1985) Wave interactions and fluid flows. Cambridge University Press, Cambridge
48. McWilliams J, Sullivan P, Moeng CH (1997) Langmuir turbulence in the ocean. *J Fluid Mech* 334:1
49. Yang D, Chen B, Chamecki M, Meneveau C (2015) Oil plumes and dispersion in Langmuir, upper-ocean turbulence: Large-eddy simulations and K-profile parameterization. *J. Geophys. Research: Oceans* 120:4729
50. Shrestha K, Anderson W, Kuehl J (2018) Langmuir turbulence in coastal zones: structure and length scales. *J Phys Oceanogr.* <https://doi.org/10.1175/JPO-D-17-0067.1>
51. Stokes G (1847) On the theory of oscillatory waves. *Trans Camb Philos Soc* 8:441
52. Mansfield J, Knio O, Meneveau C (1998) A dynamic LES scheme for the vorticity transport equation: formulation and a priori tests. *J Comp Phys* 145:693
53. Mansfield J, Knio O, Meneveau C (1999) Dynamic LES of colliding vortex rings using a 3D vortex method. *J Comp Phys* 152:305
54. Gayme D, McKeon B, Papachristodoulou A, Bamieh B, Doyle J (2010) A streamwise constant model of turbulence in plane Couette flow. *J Fluid Mech* 665:99
55. Pope S (2000) Turbulent flows. Cambridge University Press, Cambridge
56. Reynolds R, Hayden P, Castro I, Robins A (2007) Spanwise variations in nominally two-dimensional rough-wall boundary layers. *Exp Fluids* 42:311
57. Fishpool G, Lardeau S, Leschziner M (2009) Persistent Non-Homogeneous Features in Periodic Channel-Flow Simulations. *Flow Turbulence Combust* 83:823
58. Arbogast L (1800) Du calcul des dérivation. Levrault, Strasbourg
59. Goursat E (1902) Cours d'analyse mathématique. Gauthier-Villars, Paris, p 1
60. Albertson J, Parlange M (1999) Surface length scales and shear stress: implications for land-atmosphere interaction over complex terrain. *Water Resour Res* 35:2121
61. Anderson W, Meneveau C (2010) A large-eddy simulation model for boundary-layer flow over surfaces with horizontally resolved but vertically unresolved roughness elements. *Bound-Layer Meteorol* 137:397
62. Wilczek M, Stevens R, Meneveau C (2015) Spatio-temporal spectra in the logarithmic layer of wall turbulence: large-eddy simulations and simple models. *J Fluid Mech* 769:R1
63. Bou-Zeid E, Meneveau C, Parlange M (2005) A scale-dependent Lagrangian dynamic model for large eddy simulation of complex turbulent flows. *Phys Fluids* 17:025105
64. Orszag S (1970) Transform method for calculation of vector coupled sums: application to the spectral form of the vorticity equation. *J Atmos Sci* 27:890
65. Deardorff J (1970) A numerical study of 3 dimensional turbulent channel flow at large Reynolds numbers. *J Fluid Mech* 41:453
66. Piomelli U, Balaras E (2002) Wall-layer models for large-eddy simulation. *Annu Rev Fluid Mech* 34:349
67. Adrian R, Christensen K, Liu ZC (2000) Vortex organization in the outer region of the turbulent boundary layer. *Exp Fluids* 29:275
68. Anderson W (2012) An immersed boundary method wall model for high-Reynolds number channel flow over complex topography. *Int J Numer Methods Fluids* 71:1588
69. Flack K, Schultz M (2010) Review of hydraulic roughness scales in the fully rough regime. *J Fluids Eng* 132(4):041203